IMT
EPFL
ASTRON
MPIA Heidelberg
Observatoire de Genève
University of Leiden/NOVA

Astrometric Survey for Extra-Solar Planets with PRIMA
Error Budget for Astrometry
PRIMA Astrometric Observations
Technical Report

Doc. No. VLT-TRE-AOS-15753-0xxx
Issue 0.1
Date 7 Sep, 2004

Prepared . . . . . R.N. Tubbs September 8, 2004 . . . . . .
Name Date Signature

Approved . . . . . N.N. . . . . .
Name Date Signature

Released . . . . . N.N. . . . . .
Name Date Signature

Change Record

Issue	Date	Section/Parag. affected	Reason/Initiation/Documents/Remarks
0.1	7-Sep-2004	all	created

Contents

List of Figures

List of Tables

1 Overview

1.1 Scope of the Document

This represents a preliminary draft of an error budget for PRIMA narrow angle astrometry. Only a few error terms are discussed. It is clear that a large amount of work will be required to produce a complete error budget.

1.2 Work Breakdown

1.3 Critical Issues

1. Numerical simulations indicate that wavefront corrugations across the telescopes may make fringe tracking very difficult with the PRIMA FSUs (see Section 28). It will be important to do a more detailed study of this.
2. The dependence of the phase output in the two beams in StS calibration mode on atmospheric seeing and refraction effects is of some concern as this is the fundamental calibration for PRIMA astrometry. This will have to be investigated in detail to determine whether it can be solved with an appropriate observing strategy. A brief discussion is included in Sections 3 and 5.
3. The dependence of the spectral sensitivity of PRIMA on the seeing conditions due to the effect of spatial filtering, will have to be studied in detail. An accurate model of the FSU spatial filters will have to be developed in order to determine the seeing dependence of the sensitivity of PRIMA.
4. Other potential show-stoppers from items being investigated by Richard Mathar, Murakawa Koji and Rudolf Le Poole.

1.4 Identified show-stoppers

Any of the items listed in Section 1.3 could be a show-stopper.

1.5 Tools and Technologies Required

The critical issues primary involve the effects of wavefront corrugations across the aperture plane, so tools will have to be developed to investigate these in detail.

1.5.1 Data products

1.6 Questions and Requests

Further details of the design of the FSUs (spectral sensitivity, fringe tracking algorithms etc), the StS (optical quality, sharpness of roof mirror etc) and the STRAP units (Strehl ratio performance, power spectra of tip-tilt jitter etc) will be essential in producing a more realistic error budget.

1.6.1 Review Item Comment

1.6.2 Review Item Question

1.6.3 Review Item Discrepancy

1.7 Applicable Documents (ADs)

[1] V. I. Tatarski, *Wave Propagation in a Turbulent Medium*, McGraw-Hill, 1961.

[2] A. N. Kolmogorov, "Dissipation of energy in the locally isotropic turbulence," *Comptes rendus (Doklady) de l'Académie des Sciences de l'U.R.S.S.* **32**, pp. 16–18, 1941.

[3] A. N. Kolmogorov, "The local structure of turbulence in incompressible viscous fluid for very large Reynold's numbers," *Comptes rendus (Doklady) de l'Académie des Sciences de l'U.R.S.S.* **30**, pp. 301–305, 1941.

[4] D. L. Fried, "Statistics of a Geometric Representation of Wavefront Distortion," *Optical Society of America Journal* **55**, pp. 1427–1435, 1965.

[5] J. W. Keen, D. F. Buscher, and P. J. Warner, "Numerical simulations of pinhole and single-mode fibre spatial filters for optical interferometers," *Monthly Notices of the Royal Astronomical Society* **326**, pp. 1381–1386, Oct. 2001.

[6] D. F. Buscher, *Getting the most out of C.O.A.S.T. – available at http://www.mrao.cam.ac.uk/∼dfb/publications/dfbphd.pdf.* PhD thesis, Cambridge University, 1988.

[7] D. Buscher, "Optimizing a ground-based optical interferometer for sensitivity at low light levels," *Monthly Notices of the Royal Astronomical Society* **235**, pp. 1203–1226, Dec. 1988.

[8] D. Saint-Jacques, *Astronomical Seeing in Space and Time – available at http://olbin.jpl.nasa.gov/theses/dsj-thesis.ps.* PhD thesis, Cambridge University, 1998.

[9] L. A. D'Arcio, *Selected aspects of wide-field stellar interferometry.* PhD thesis, Technische Universiteit Delft, 1999.

[10] F. Roddier, J. M. Gilli, and G. Lund, "On the origin of speckle boiling and its effects in stellar speckle interferometry," *Journal of Optics* **13**, pp. 263–271, Oct. 1982.

[11] C. Aime, J. Borgnino, F. Martin, R. Petrov, and G. Ricort, "Contribution to the space-time study of stellar speckle patterns," *Optical Society of America, Journal, A: Optics and Image Science* **3**, pp. 1001–1009, July 1986.

[12] R. J. Mathar, "Calculated Refractivity of Water Vapor and Moist Air in the Atmospheric Window at 10μm," *Applied Optics* **43**, pp. 928–932, Feb. 2004.

[13] F. Zernike, "Diffraction theory of the knife-edge test and its improved form, the phase-contrast method," *Physica* **1**, pp. 689–704, 1934.

[14] F. Zernike, "Diffraction theory of the knife-edge test and its improved form, the phase-contrast method," *Monthly Notices of the Royal Astronomical Society* **94**, pp. 377–384, Mar. 1934.

[15] R. Launhardt, S. Frink, D. Segransan, and J. Setiawan, "Astrometric survey for extra-solar planets with prima: Scientific proposal," Tech. Rep. Planets-PRI-SCI-0001, DDL consortium – ESO, Geneva Observatory, Leiden Observatory, MPIA Heidelberg, Sept. 2003.

[16] L. B. Venema, H. Baumeister, P. Bizenberger, R. Launhardt, H. Hanenburg, J. Pragt, D. Gillet, L. Sache, R. Wüthrich, P. Müllhaupt, M. Fleury, D. Sosnowska, O. Scherler, and R. N. Tubbs, "Astrometric survey for extra-solar planets with prima: Technical proposal," Tech. Rep. Planets-PRI-SCI-0002, DDL consortium – ESO, Geneva Observatory, Leiden Observatory, MPIA Heidelberg, Sept. 2003.

[17] P. E. Ciddor, "Refractive index of air: new equations for the visible and near infrared," *Applied Optics* **35**, pp. 1566–1573, 1996.

[18] P. E. Ciddor and R. J. Hill, "Refractive index of air 2: Group index," *Applied Optics* **38**, pp. 1663–1667, 1999.

[19] K. P. Birch and M. J. Downs, "Correction to the updated edlén equation for the refractive index of air," *Metrologia* **31**, pp. 315–316, 1994.

[20] J. Beers and T. Doiron, "Verification of revised water vapour correction to the refractive index of air," *Metrologia* **29**, pp. 315–316, 1992.

[21] K. P. Birch and M. J. Downs, "The result of a comparison between calculated and measured values of the refractive index of air," *Journal of Physics E* **21**, pp. 694–695, 1988.

[22] K. E. Erickson, "Investigation of the invariance of atmospheric dispersion with a long path interferometer," *Journal of the Optical Society of America* **52**, pp. 777–780, July 1962.

1.8 Acronyms

ASTRON	Stichting Astronomisch Onderzoek in Nederland `http://www.astron.nl/`
AD *n*, *m*	Reference to Applicable Documents n and m (see Section 1.7)
AO	Adaptive Optics
AT	Auxiliary Telescope (of the VLTI)
DDL	Differential Delay Line
EPFL	École Polytechnique Fédérale de Lausanne `http://www.epfl.ch/`
ESO	European Southern Observatory `http://www.eso.org/`
MACAO	Multi Application Curvature Adaptive Optics
PS	Primary Star
PSF	Point Spread Function
S/N	Signal-to-noise ratio (signal / noise)
SeS	Secondary Star
STRAP	Tip-tilt corrector at the Auxiliary Telescopes
StS	Star Separator
VLTI	Very Large Telescope Interferometer `http://www.eso.org/projects/vlti/`

2 Introduction

2.1 Background

Producing an error budget for PRIMA astrometric observations will be a long and complicated process. In order to break up the work, the error calculation has been separated into a number of principle terms, with each term getting a section (or appendix) in this document. Each of these sections provides an introduction to the error term. A little more detail has been provided for some of the error terms, where that information was already available in existing documents. A substantial amount of further work will be required in order to complete the error budget.

One of the most difficult tasks has been to find the interdependencies of each of the different error terms. If one term in the error budget calculation is changed, this list of interdependencies can be used to work out which other components of the error budget calculation will be effected by the change. Tables of interdependencies can be seen in Appendix O. These include both direct dependencies (the terms in the error budget which are directly effected by a change) and indirect dependencies (those terms which are effected indirectly through a change in an intermediate term in the calculations).

In order to introduce the terminology used in this report I will first give an introduction to atmospheric turbulence and interferometry. In the standard classical theory, light is treated as an oscillation in a field ψ. For monochromatic plane waves arriving from a distant point source with wave-vector $\mathbf{k}$:

$$\psi_u(\mathbf{r},t) = A_u e^{i(\phi_u + 2\pi\nu t + \mathbf{k}\cdot\mathbf{r})} \tag{1}$$

where ψ_u is the complex field at position $\mathbf{r}$ and time t, with real and imaginary parts corresponding to the electric and magnetic field components, ϕ_u represents a phase offset, ν is the frequency of the light determined by $\nu = c\,|\mathbf{k}|\,/\,(2\pi)$, and A_u is the amplitude of the light.

The photon flux in this case is proportional to the square of the amplitude A_u, and the optical phase corresponds to the argument of the complex variable ψ_u. As wavefronts pass through the Earth's atmosphere they may be perturbed by refractive index variations in the atmosphere. Figure 1 shows schematically a turbulent layer in the Earth's atmosphere perturbing planar wavefronts before they enter a telescope. The perturbed wavefront ψ_p may be related at any given instant to the original planar wavefront $\psi_u(\mathbf{r},t)$ in the following way:

$$\psi_p(\mathbf{r},t) = \left(\chi_p(\mathbf{r},t)\, e^{i\phi_p(\mathbf{r},t)}\right)\psi_u(\mathbf{r},t) \tag{2}$$

where $\chi_p(\mathbf{r},t)$ represents the fractional change in wavefront amplitude and $\phi_p(\mathbf{r},t)$ is the change in wavefront phase introduced by the atmosphere. From here on in this document, $\phi_p(\mathbf{r},t)$ will be called the optical phase (although strictly it is the *perturbation* in the optical phase in comparison to an unperturbed light beam). Similarly, in discussions of atmospheric effects $\chi_p(\mathbf{r},t)$ will be called the wavefront amplitude although it is actually a normalised form of the amplitude.

A description of the nature of the wavefront perturbations introduced by the atmosphere is provided by the *Kolmogorov model* developed by Tatarksi (AD 1) and Kolmogorov (AD 2, 3). This model is supported by a variety of experimental measurements and is widely used in simulations of astronomical instruments. The model assumes that the wavefront perturbations are brought about by variations in the refractive index of the air. These refractive index variations lead directly to phase fluctuations described by $\phi_p(\mathbf{r},t)$, but any amplitude fluctuations are only brought about as a second-order effect while the perturbed wavefronts propagate from the perturbing atmospheric layer

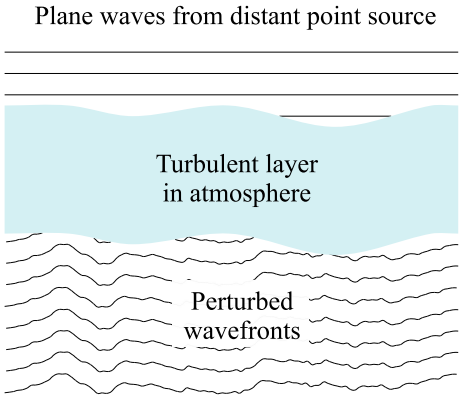

Figure 1: Schematic diagram illustrating how optical wavefronts from a distant star may be perturbed by a turbulent layer in the atmosphere. The vertical scale of the wavefronts plotted is highly exaggerated.

to the telescope. The performance of interferometers is dominated by the phase fluctuations $\phi_p(\mathbf{r}, t)$, although the amplitude fluctuations described by $\chi_p(\mathbf{r}, t)$ introduce intensity variations (scintillation) in the interferometric signal.

The spatial phase fluctuations at an instant in time in a Kolmogorov model are usually assumed to have a Gaussian random distribution with the following second order structure function:

$$D_{\phi_p}(\rho) = \left\langle \left| \phi_p(\mathbf{r}) - \phi_p(\mathbf{r}+\rho) \right|^2 \right\rangle_{\mathbf{r}} \tag{3}$$

where $D_{\phi_p}(\rho)$ is the atmospherically induced variance between the phase at two parts of the wavefront separated by a distance ρ in the aperture plane, and $\langle \ldots \rangle$ represents the ensemble average.

The structure function of AD 1 can be described in terms of a single parameter r_0:

$$D_{\phi_p}(\rho) = 6.88 \left(\frac{|\rho|}{r_0} \right)^{5/3} \tag{4}$$

r_0 indicates the "strength" of the phase fluctuations as it corresponds to the diameter of a circular telescope aperture at which atmospheric phase perturbations begin to seriously limit the image resolution. Typical r_0 values for K band (2.2 μm wavelength) observations at good sites are 40—90 cm. Fried (AD 4) noted that r_0 also corresponds to the aperture diameter d for which the variance σ^2 of the wavefront phase averaged over the aperture comes approximately to unity:

$$\sigma^2 = 1.0299 \left(\frac{d}{r_0} \right)^{5/3} \tag{5}$$

Equation 5 represents a commonly used definition for the atmospheric coherence length r_0.

2.2 Interferometry

An interferometer typically consists of a number of sub-apertures positioned in a plane. Movements of the sub-apertures are used to produce a larger synthesized aperture plane. The aim of an interferometer is to measure the cross-correlation between the electric field measured at different points

in the synthesized aperture plane. Light is collected with two or more sub-apertures (typically telescopes or siderostats) and a wavelength range is selected using optical filters. The simplest form of cross-correlation for an interferometer with two sub-apertures (and the fundamental goal of a measurement with a PRIMA FSU) is the correlated flux C from the star:

$$C = \psi_{u1}\psi_{u2}^{*} \tag{6}$$

where ψ_{u1} and ψ_{u2} are the complex electric field amplitudes from the two sub-apertures produced by the star, and * indicates the complex conjugate. In VLTI/PRIMA the wavefronts from the star are spatially filtered (see AD 5 for a discussion of spatial filtering). This means that the flux from a single point in the image plane of each sub-aperture is selected, in contrast to the optical field as a function of position in the aperture plane described by $\psi_u(\mathbf{r}, t)$ in Equation 1. In reality C varies with time due to the change in projected baseline as the Earth rotates. In this discussion I will ignore the effects of Earth rotation on the projected baseline, which is adequate when describing a short astronomical observation.

The Earth's atmosphere introduces rapid fluctuations in the optical path length from an astronomical source to the two apertures, as discussed in Section 2.1. For monochromatic observations these optical path fluctuations can be described in terms of phase rotations $\phi_{p1}(t)$ and $\phi_{p2}(t)$ to ψ_{u1} and ψ_{u2} respectively in Equation 6 (in a similar way to Equation 2 in the aperture plane description). These phase rotations result in fluctuations in the phase of the correlated flux C. Again the amplitude fluctuations can be described by $\chi_{p1}(t)$ and $\chi_{p2}(t)$. Our description of the atmospherically perturbed correlated flux $C'(t)$ then looks like this:

$$\begin{aligned} C'(t) &= C\left(\chi_{p1}(t)\, e^{i\phi_{p1}(t)}\right)\left(\chi_{p2}(t)\, e^{i\phi_{p2}(t)}\right)^{*} && (7)\\ &= CA(t)\, e^{i\theta(t)} && (8)\end{aligned}$$

where $i = \sqrt{-1}$ and t is the time. $A(t)$ and $\theta(t)$ describe the amplitude and phase fluctuation introduced into the (complex) correlated flux by the atmosphere, and are given by:

$$\begin{aligned} A(t) &= \chi_{p1}(t)\,\chi_{p2}(t) && (9)\\ \theta(t) &= \phi_{p1}(t) - \phi_{p2}(t) && (10)\\ & && (11)\end{aligned}$$

The timescale over which the RMS change in the phase $\theta(t)$ at any given point is ~ 1 radian is called the coherence time t_c of the interference fringes. Each measurement of $C'(t)$ must be made within one coherence time in order to avoid the measurements being corrupted by phase fluctuations.

VLTI PRIMA can observe two different stars simultaneously. One PRIMA FSU measures the correlated flux $C'_{PS}(t)$ from the Primary Star (PS), and the other the correlated flux $C'_{SeS}(t)$ on the Secondary Star (SeS).

2.2.1 Narrow angle astrometry

The aim of the PRIMA astrometry program is to accurately measure the angular separation of stars which have small angular separations. This is possible using an interferometer as the atmosphere applies similar perturbations to both stars when the angular separation is small. For example the first star (PS) could have a correlated flux C_{PS} and atmospheric phase perturbation $\theta(t)$ and the

second star (*SeS*) a correlated flux C_{SeS} and atmospheric phase perturbation $\theta(t) + \Delta\theta(t)$, giving atmospherically perturbed correlated fluxes of:

$$C'_{PS}(t) = C_{PS}A_{PS}(t)\exp(i\theta(t)) \quad (12)$$

$$C'_{SeS}(t) = C_{SeS}A_{SeS}(t)\exp(i[\theta(t) + \Delta\theta(t)]) \quad (13)$$

Note that $\Delta\theta(t)$ fluctuates randomly with zero mean. If the variance over time of $\Delta\theta$, $\left\langle |\Delta\theta(t)|^2 \right\rangle_t < 1$ we are said to be in the isoplanatic regime (where the fringe differential phase is small). The mean difference in the phase of the correlated fluxes for the two stars is then related directly to the astrometric separation of the stars.

There are two general approaches to long baseline interferometry which I will call phase stabilised interferometery and non-phase stabilised interferometery.

2.2.2 Non phase-stabilised interferometry

Many existing interferometers (e.g. SUSI, COAST, IOTA, VINCI) are not phase stabilised. These interferometers measure observables which are not affected by atmospheric phase changes, so that it is not necessary to track the atmospheric phase fluctuations. The principle benefit of this is that a bright reference star is *not* required as the observables can be integrated over many fringe coherence times. Example observables include the visibility amplitude and the bispectrum or "triple-produce" (the phase of the bispectrum known as the closure phase is more often discussed, but the bispectrum is the fundamental observable).

2.2.3 Non phase-stabilised operation of PRIMA

In order to perform non phase-stabilised operation we must measure an observable which is not strongly affected by atmospheric phase changes. The simplest example is $C'_{PS}C'^{*}_{SeS}$:

$$C'_{PS}C'^{*}_{SeS} = C_{PS}A_{PS}(t)\exp(i\theta(t))\,C_{SeS}A_{SeS}(t)\exp(-i[\theta(t) + \Delta\theta(t)]) \quad (14)$$

$$= C_{PS}C_{SeS}A_{PS}(t)\,A_{SeS}(t)\exp(-i\Delta\theta(t)) \quad (15)$$

In the isoplanatic regime, $\left\langle |\Delta\theta(t)|^2 \right\rangle_t < 1$ and varies randomly about zero, so we can obtain an accurate measurement of $C_{PS}C^{*}_{SeS}$ by integrating $C'_{PS}C'^{*}_{SeS}$ over many fringe coherence times. $C_{PS}C^{*}_{SeS}$ is of great interest, as the phase of this number can be used to calculate the separation of the stars (the phase of $C_{PS}C^{*}_{SeS}$ is commonly called the *astrometric phase*, although it is the complex number $C_{PS}C^{*}_{SeS}$ which is the principle observable – a similar situation to the case of the bispectrum). The integration of $C_{PS}C^{*}_{SeS}$ can be improved by weighting each measurement of $C'_{PS}C'^{*}_{SeS}$ by an estimate of the S/N for that measurement.

In order to obtain a measurement of $C'_{PS}C'^{*}_{SeS}$ with good S/N in a reasonable period of time, both stars must provide a S/N ratio of $\gtrsim 0.1$ for measurements of the correlated flux C.

2.2.4 Phase-stabilised interferometry

The NPOI and PTI interferometers actively track and compensate for atmospheric phase fluctuations. A bright reference star is required in order to do this typically providing a S/N of $\gtrsim 10$ for measurements of the correlated flux C_{PS} on the PS. Once the fringes are stabilised, faint signals which are phase-correlated with the fringes can be coherently integrated.

2.2.5 Phase-stabilised operation of PRIMA

Measurements of the atmospherically induced phase perturbations can be made on a bright star ($\theta(t)$ in Equations 12 and 14) and then the optical path length from the both stars can be physically adjusted (typically using movable mirrors) to remove the term $\theta(t)$ from the phase perturbations from both stars. For star (SeS) we get:

$$C'_{SeS} = C_{SeS} \exp\left(i\Delta\theta(t)\right) \tag{16}$$

In the isoplanatic regime, $\left\langle |\Delta\theta(t)|^2 \right\rangle_t < 1$ so the fringes on star (SeS) will remain stable to within ~ 1 radian over long periods of time. This means that the fringe signal for star (SeS) can be integrated on the detector over many atmospheric coherence times. In practice the maximum integration time in the infrared is limited by detector saturation from the thermal background, but the S/N for fringe measurements on the faint star (SeS) will be a few times larger than for the non phase-stabilised case discussed in Section 2.2.3.

In this mode of operation, $C'_{PS}C'^{*}_{SeS}$ can be calculated in the same way as in Section 2.2.3, providing information about the angular separation of the stars. Note that the phase of $C'_{PS}C'^{*}_{SeS}$ (the *astrometric phase*) is only a useful parameter when the S/N ratio of $C'_{PS}C'^{*}_{SeS}$ is greater than unity, so that for faint (SeS) stars $C'_{PS}C'^{*}_{SeS}$ must be integrated as a complex number until the S/N ratio is greater than one *before* the astrometric phase is calculated. This has important implications for the software running the PRIMA FSUs.

2.2.6 Limitations due to PRIMA hardware

The current design of the PRIMA FSU hardware should be compatible with both phase-stabilised operation (Section 2.2.5) and non phase-stabilised operation (Section 2.2.3). The low spectral resolution of the FSUs is slightly better optimised for phase-stabilised operation, however. If the data transfer architecture at the VLTI precludes the use of $C'_{PS}C'^{*}_{SeS}$ as the primary observable for PRIMA, non phase-stabilised operation will be impossible and the limiting magnitude for phase-stabilised operation will be slightly poorer. For the remainder of this document I will assume that astrometric measurements are based on $C'_{PS}C'^{*}_{SeS}$ provided from both phase-stabilised operations and non phase-stabilised operations of PRIMA.

2.2.7 Extension to a finite bandpass

Sections 2.2.1 to 2.2.5 are only strictly applicable at a single wavelength (i.e. for a monochromatic observation). The PRIMA FSUs utilize one broad channel and two narrow channels which together cover the K band (from ~ 1.95 μm to ~ 2.45 μm). Due to the refractive properties of the atmosphere, each wavelength within the K band follows a slightly different path through the atmosphere. Light of different wavelengths reaching the aperture plane will have passed through slightly different parts of the turbulent layers in the atmosphere. The optical phase offset ϕ at each wavelength depends on both the mean phase across each telescope aperture and on the corrugations in the phase across each of the telescope apertures. The phase rotation $\phi(\mathbf{r}, t, \lambda)$ (cf. Equation 2) in the aperture plane induced by a high-altitude atmospheric layer, at a given wavelength λ and at a given time t and position $\mathbf{r}$ in the AT aperture are dependent on the fluctuation in delay induced by the atmospheric turbulence $\Delta z(\mathbf{r}' + \mathbf{\Delta r}'(\lambda), t, \lambda)$ as follows:

$$\phi(\mathbf{r}, t, \lambda) = \frac{\Delta z(\mathbf{r}' + \mathbf{\Delta r}'(\lambda), t, \lambda)}{\lambda} \tag{17}$$

where $\mathbf{r}'$ is the projection of $\mathbf{r}$ along the line of sight towards the star up to the layer of turbulence, and $\boldsymbol{\Delta}\mathbf{r}'(\lambda)$ is the wavelength-dependent offset from this path induced by bulk atmospheric refraction (the time delay for light propagation can be ignored).

In order to make measurements with high S/N ratio, the gradient of phase with wavelength must be minimised in the PRIMA FSU spectral channels. The phase difference between the correlated fluxes in the spectral channels at the edges of the K band is minimised through adjustments of the VLTI delay lines (group delay tracking). Note that it is the phase of $C_{PS}C^*_{SeS}$ for the central spectral channel which will be used for astrometry (i.e. the phase difference between the fringes on the two stars in the central spectral channel). The group delay will not be used for astrometric measurements as it cannot be measured as accurately as the phase of $C_{PS}C^*_{SeS}$, and because existing models for the refractive index of air provide lower accuracy when converting the group delay into the separation of the stars.

3 Numerical simulations

3.1 Introduction

Apart from a few simple cases such as an interferometer with pointlike apertures (see e.g. AD 6, 7) or an interferometer with ideal AO correction (e.g. AD 8, 9), the only approach which can be used to analyse the temporal properties of interferometric fringes is that of numerical simulation. Numerical simulations are also required to investigate specialised components in interferometers such as spatial filters (e.g. AD 5). For this reason, numerical studies have often played an important role in studies of interferometer performance or design (e.g. AD 6).

Numerical simulations were required in the preliminary stages of the error budget preparation for PRIMA in order to obtain order-of-magnitude estimates for many of the complicated error terms and highlight those which might be problematic. In order to minimise the time invested, existing atmospheric simulations were used with the minimum modification required for useful estimates of terms in the PRIMA error budget. More realistic simulations may be required at a later date to study in detail error terms which are expected to have a significant impact on the overall performance of PRIMA.

3.2 Simulation method

The simulations utilised a wind-scatter model of the atmosphere (see e.g. AD 10) using two Taylor screens of frozen Kolmogorov turbulence with large ($> 1000 r_0$) outer scale. Fluctuations in air and water vapour spectral dispersion were not modelled, and the Taylor screens introduced equal fluctuations in the wavefront delay at all wavelengths.

In the simulations, the Taylor screens were blown past the simulated telescopes at constant wind velocities. The timescale for changes in the light intensity measured with a large diameter telescope is proportional to the parameter $(r_0/\Delta v)$ (see AD 10, 11) where Δv is the standard deviation of the distribution of the wind velocities for the screens, weighted by the turbulence C_N^2 for each screen:

$$\Delta v = \left[\frac{\int_0^\infty |\mathbf{v}\,(h)|^2 \, C_N^2\,(h)\,\mathrm{d}h}{\int_0^\infty C_N^2\,(h)\,\mathrm{d}h} - \left| \frac{\int_0^\infty \mathbf{v}\,(h)\, C_N^2\,(h)\,\mathrm{d}h}{\int_0^\infty C_N^2\,(h)\,\mathrm{d}h} \right|^2 \right]^{1/2} \tag{18}$$

and using the same definitions for the layer height h, the wind velocity $\mathbf{v}$ and the turbulence strength C_N^2 as Roddier (AD 10).

The Taylor screens were moved across the telescope aperture at the appropriate wind speeds along one axis of the rectangular Taylor screen array. A section of each Taylor screen was extracted at each time point and then rotated according to the wind direction angle and re-sampled to have at least twice as many pixels per r_0 using linear interpolation to minimise pixel aliasing. The resulting screens were summed and converted to complex wavefronts at a range of different wavelengths. After truncating the wavefronts with a circular telescope aperture, an image plane representation of the wavefronts was generated at each wavelength using an FFT. The atmospheric model used throughout this documents had two Taylor screens of equal strength moving at equal wind speed with wind angles differing by 120°. The time unit used when describing the simulations corresponds to the time taken for each of the Taylor screens to move by the coherence length r_0 for the wavefronts in the telescope aperture plane (after the wavefronts had been perturbed by both atmospheric layers).

Seven discrete wavelength channels were simulated, with equal spacings in wavelength between 1.97 μm and 2.43 μm. The correlated fluxes in the seven wavelength channels were then linearly combined to give three channels with wavelengths and bandpasses approximately matching the channels on the real PRIMA FSUs.

In some of the simulations, bulk atmospheric refraction and/or scintillation were also modelled. For these studies one of the Taylor screens was assigned an altitude of 500 m above the telescope and the other 5000 m. For refraction studies Snell's law was used to model the variation of the light ray position and tilt with wavelength and altitude, ensuring that the correct part of each Taylor screen was used for each wavelength channel. This was calculated using the approach introduced in Section 2.2.7.

The fluctuation in delay induced by the atmospheric turbulence ($\Delta z\left(\mathbf{r}' + \mathbf{\Delta r}'\left(\lambda\right), t, \lambda\right)$ from Equation 17) has only a small direct dependence on wavelength λ (due to dispersion), so the induced phase rotation is well approximated across the K band by:

$$\phi\left(\mathbf{r}, t, \lambda\right) = \frac{\Delta z\left(\mathbf{r}' + \mathbf{\Delta r}'\left(\lambda\right), t, \lambda_{cen}\right)}{\lambda} \tag{19}$$

where $\Delta z\left(\mathbf{r}' + \mathbf{\Delta r}'\left(\lambda\right), t, \lambda_{cen}\right)$ is the delay induced by atmospheric fluctuations at the centre of the K band (wavelength λ_{cen}) at position $\mathbf{r}' + \mathbf{\Delta r}'\left(\lambda\right)$ and time t. This approximation was utilised in all the numerical simulations of the effects of seeing on astrometric performance presented in this document. Note that in accurate calculations of the effect of atmospheric refraction and dispersion these simplifications should *not* be used.

For the simulations, the air density as a function of altitude was based on the Glenn Research Center's *Earth Atmosphere Model*, and the refractive index was calculated from the density using a cubic spline fit to K-band data from AD 12. The algorithms used are presented in Figures 2 and 3. The optical ray displacement was calculated and integrated at 50 m intervals through the atmosphere – Richard Mathar has recently started work on an improved model for the optical path through the atmosphere.

For the scintillation studies a first-order approximation to the optical propagation was performed. The effect of each Taylor screen was investigated independently, with the amplitude fluctuation ($\chi_p\left(\mathbf{r}, t\right)$ from Equation 2) in the AT aperture plane estimated by applying phase changes in the conjugate plane to re-image the Taylor screen to the appropriate altitude. The amplitude fluctuations from the two Taylor screens were then combined multiplicatively without taking account of any second-order terms resulting from the interaction of the wavefront fluctuations induced by the two Taylor screens. The phase changes resulting from optical propagation from the turbulent layers to the telescopes were also ignored.

The spatial sampling of the electric field was kept constant in the image plane for all the simulations which necessarily required wavelength-dependent spatial sampling in the pupil plane.

3.3 Simulation Results

The simulations discussed in this section are widely used throughout the remainder of the document. A few very basic results are presented here to provide a better understanding of the simulations and of the variation of the optical wavefront properties with position in the image plane.

Figure 4 shows the short exposure image quality expected when using an AT to look at a point source 30° above the horizon under mediocre conditions. The effects of atmospheric refraction were ignored

```
/* Height is in metres, density is in kg/m^3 */

float air_density(float height)
{
  float t;
  float p;
  float rho;

  if (height<11000.0) {
    t=15.04-0.00649*height;
    p=101.29*pow((t+273.1)/288.08,5.256);
  }
  else {
    t=-56.46;
    p=22.65*exp(1.73-0.000157*height);
  }
  rho=p/(0.2869*(t+273.1));

  return(rho);

}
```

Figure 2: Algorithm used to estimate air density as a function of altitude for simulations of atmospheric seeing effects

```
/* Height is in metres and wavelength is in microns */

float n_minus_1(float wavelength, float height)
{
  float n_minus_1;
  float density;
  float air_density(float height);

  n_minus_1 = -1.434E-07*(wavelength-2.0)*(wavelength-2.0)*(wavelength-2.0)
    +2.2568E-07*(wavelength-2.0)*(wavelength-2.0)
    -2.9281E-07*(wavelength-2.0)
    +2.031756E-04;

  density=air_density(height);

  return(n_minus_1*density/0.945404);

}
```

Figure 3: Algorithm used to estimate refractivity as a function of altitude and wavelength for simulations of atmospheric seeing effects

Figure 4: Simulated short exposure image through an AT pointing at the zenith with $4r_0$ across the aperture diameter.

Figure 5: Identical to Figure 4 but including the effects of atmospheric refraction for a zenith angle of 60 degrees.

The three FSU spectral channels are shown in red, green and blue.

when generating this image. Note that the image is *coloured* – this means that the spectral energy distribution reaching the detectors will depend strongly on the position of the FSU spatial filter (or in other words on the tip-tilt error). If the StS is put into calibration mode, the light from one half of the PSF will be sent to one FSU, and the light from the other half of the PSF will be sent to the other PSF. The colour of the light sent to the two FSUs will be different, and hence the astrometric measurements on the two FSUs will also be different. The average colour of the light reaching the FSUs will vary with the seeing conditions and with the performance of the STRAP unit (as the size and shape of the mean PSF is strongly wavelength dependent).

Figure 5 is identical to Figure 4 except that atmospheric refraction has been "switched on" (including both the lateral shift of the beam in the atmosphere and the change in the angle-of-arrival with wavelength). Note that the colours are slightly different to the case with atmospheric refraction switched off (Figure 4). As the angle of refraction remains relatively constant with time during an observation, this colour shift will be systematically applied to a whole observation. If the StS is put into calibration mode, the two FSUs will receive light which has systematically different colours (and hence systematically different astrometric observables). As the flux distribution in the image depends on the seeing, the magnitude of the colour difference between the two channels will vary with the seeing conditions (i.e. on timescales of minutes and hours). This will lead to drifts in the differential phase between the two beams on similar timescales. In order to calibrate out this effect, the atmospheric seeing, STRAP unit performance, air density and humidity may have to be monitored at the ATs, particularly when using the StS calibration mode. A good knowledge of the coupling of the FSU spatial filter as a function of image-plane position and wavelength will be required for such a simulation. If the StS roof mirror is aligned with the direction of the bulk atmospheric dispersion the systematic effects may be substantially reduced.

Another area where numerical simulations are essential is in the assessment of fringe tracking performance when there are wavefront corrugations across the AT apertures. In early optical interferometers the apertures were usually stopped-down in order to keep the variance in the wavefront phase across the aperture below ~ 1 radian. With the introduction of spatial filters larger aperture sizes have come into common usage, and hence the variance of the wavefront phase is often much larger than 1 radian. It will be important to assess the effect of these wavefront corrugations on the temporal properties of the interferometric fringes and hence determine the expected fringe tracking performance. In order to highlight the detrimental effect of wavefront corrugations, maps of the optical phase and intensity in the image plane of a single telescope are shown for a large ($9r_0$) aperture in Figure 6 for a series of closely-spaced time-steps. Each speckle in the image plane has a different (random) phase, and the speckles in the image change rapidly. If a spatial filter was used to select light from one speckle and use it in an interferometer, the phase of the light would vary as quickly as the phases of the speckles in the image plane. This is in stark contrast to the piston mode component (see e.g. AD 9) which in this case does not change significantly from one time-step to the next, and thus contributes little to the high-frequency fluctuations in the fringe phase.

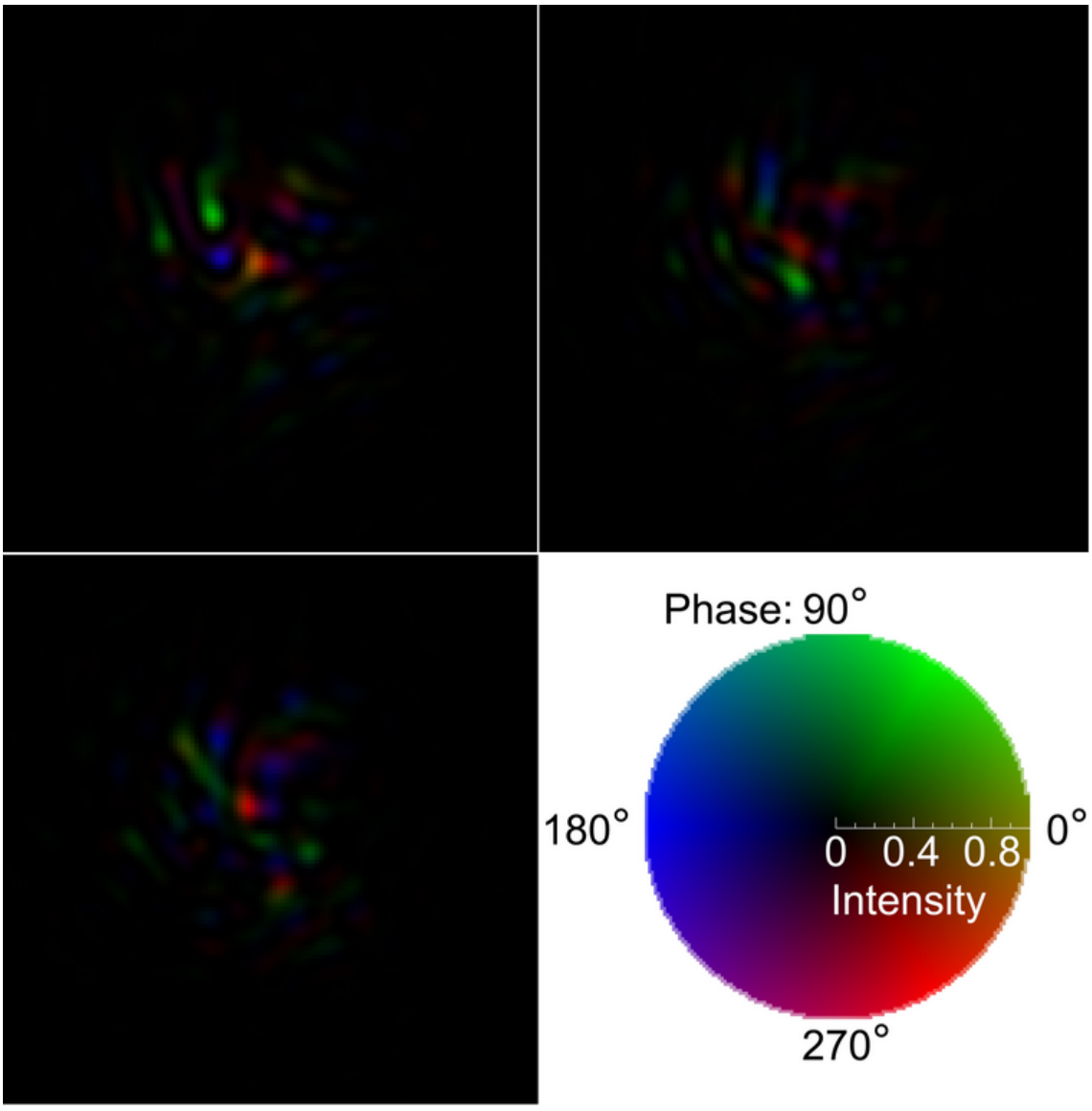

Figure 6: Phase and light intensity as a function of position in the image plane for a $9r_0$ diameter aperture. Three closely-separated time-points are shown starting on the top row (the piston mode changes by < 1 radian over the total time shown). The legend at the lower right indicates the dependence of *hue* and *brightness* on optical phase and intensity respectively.

4 Wavefront amplitude and phase fluctuations above M1

4.1 Introduction

This section of the error budget intends to describe the optical wavefront amplitude and phase immediately before M1 sufficiently well that the simulations of the internal properties of the VLTI can be de-coupled from simulations of the atmosphere. Also included in this section is a discussion of the beam walk at high altitude resulting from bulk atmospheric refraction, as this can be separated from the details of the atmospheric seeing simulations.

The simulations described in Section 3 were used to investigate the approximate level of perturbation introduced into the optical wavefronts by the atmosphere. One of the main complexities in the design and operation of PRIMA is the wavelength dependence of the wavefront corrugations across the telescope pupil, and the resulting wavelength-dependent perturbations to the fringe phase induced by atmospheric seeing (further details of this can be found in Section 28). This results from the wavelength dependence of the phase perturbations caused by atmospheric seeing which are described as a function of position in the AT aperture plane by Equation 17.

In order to illustrate the wavelength dependence of seeing effects, I have plotted various wavefront properties in the first timestep of the simulations. The wavefronts at M1 were not directly output from the simulations, only the resulting wavefronts after tip-tilt correction had been performed (subtracting the tip-tilt Zernike modes). Figures 7 and 8 show the delay applied to the wavefronts by the atmosphere after the tip-tilt correction. Figure 7 shows the case for 1.97 μm wavelength and Figure 8 the case for 2.43 μm wavelength. Note that apart from the pixel sampling in the images there is no obvious difference. This is because the delay Δz from Equation 19 has only a weak dependence on wavelength.

A larger difference appears when the atmospheric delays are converted into optical amplitude and phase. The amplitude and phase in the pupil plane are shown in Figures 9 and 10 for the same timestep as used for Figures 7 and 8. Figure 9 shows the amplitude and phase at 1.97 μm wavelength plotted as a function of position in the AT aperture plane. The discontinuities in the phase occur when the phase wraps around by 2π radians. The same plots are shown in Figure 10 for 2.43 μm wavelength. It is clear that the phase perturbations are much more severe at 1.97 μm due to the inverse relationship of the phase ϕ with wavelength seen in Equation 19.

Example plots from 4 later timesteps of the simulations are shown in Figures 13 and 14.

Figure 13 shows the delay imposed on the wavefronts by the simulated atmosphere as a function of position in one of the AT aperture planes. The tip-tilt within the AT aperture has been corrected by perfectly compensating the tip and tilt Zernike modes, resulting in a discontinuity at the edges of the aperture in this plot. The four images show four timesteps with the atmospheric phase screens moving by $r_0/4$ in consecutive images in the directions described in Section 3. Each atmospheric layer has an equal effect on the wavefront phase.

Figure 14 shows the optical amplitude as a function of position in the same AT aperture plane. It is clear that the amplitude fluctuations are dominated by one of the layers moving from the lower left to the upper right. The dominant layer is the higher one (5 km above the telescope – see Section 3.2).

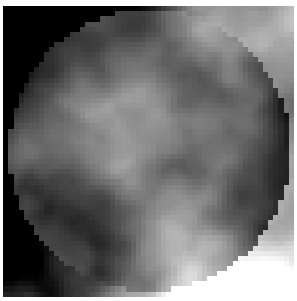

Figure 7: Atmospherically induced optical delay at one timepoint as a function of position in one AT aperture plane at 1.97 μm wavelength.

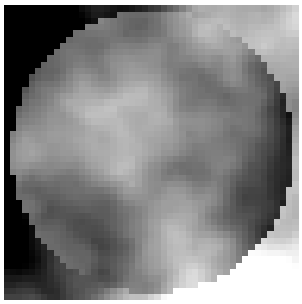

Figure 8: Optical delay at 2.43 μm wavelength at the same timepoint.

In both plots the tip-tilt Zernike modes have been corrected across the telescope aperture, resulting in a discontinuity at the edge of the aperture.

4.2 Dependencies

4.2.1 This error term is effected by

Error term	Relevant subsection
Temporal and spatial properties of seeing at Paranal	A.3
Temporal intermittency of seeing	D.3
Isoplanatism at Paranal	D.3
Separation of stars	L.3.2
Observing parameters	N.3

4.2.2 Error terms effected by this

Error term	Relevant subsection
Limiting magnitudes for PRIMA	29.3
Fringe jumps and group tracking errors	28.3
Wavefront corrugations before and after the StS	5.3
Atmospheric scintillation and thermal background fluctuations	9.3
Effect of aberrations in image plane optical components	20.3
Effect of aberrations in pupil plane optical components	23.3
VLTI baseline geometry	15.3
Effect of beam walk on optics before the Star Separator	24.3
Systematic differences in baseline length for primary and secondary star	16.3

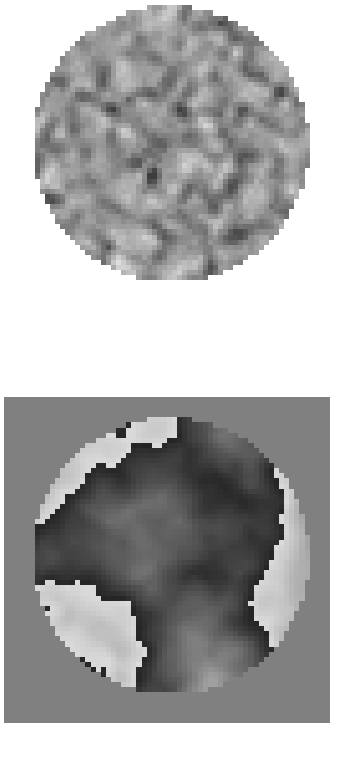

Figure 9: Optical amplitude (upper panel) and phase in the AT aperture plane at 1.97 μm wavelength. The discontinuities in the phase are due to the phase wrapping through 2π radians.

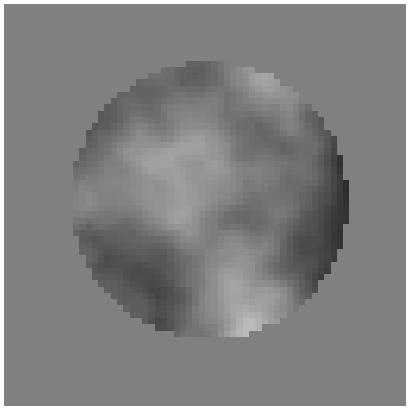

Figure 10: Optical amplitude and phase in the AT aperture plane at 2.43 μm wavelength.

These plots were produced from the wavefront corrugations shown in Figures 7 and 8. Note that larger amplitudes appear darker in the greyscale plots.

Figure 11: Intensity in the image plane at 1.97 μm wavelength

Figure 12: Intensity in the image plane at 2.43 μm wavelength

These plots were produced from the amplitude and phase data in Figures 9 and 10.

4.3 Detailed contributions

sect:ctb-1-1-1-seeing

The largest contribution from atmospheric seeing on the measured astrometric parameters will be a zero mean process. Isoplanaticity will be the principle limitation on the separation of target star and reference star. Systematic errors in the astrometry can be generated in the StS calibration mode through a combination of seeing fluctuations and atmospheric refraction away from the zenith. This would encourage the use of an observing strategy where the PS and SeS were switched regularly between alternate FSUs.

Atmospheric seeing is introduced through the combination of:

1. Atmospheric turbulence, typically between shearing wind layers
2. Fluctuations in the density of air or in the density of water vapour, due to changes in temperature, humidity and to a much lesser extent pressure

4.4 Impact on astrometry

4.5 Corrective measures required

4.6 Further analysis required

4.7 Conclusion

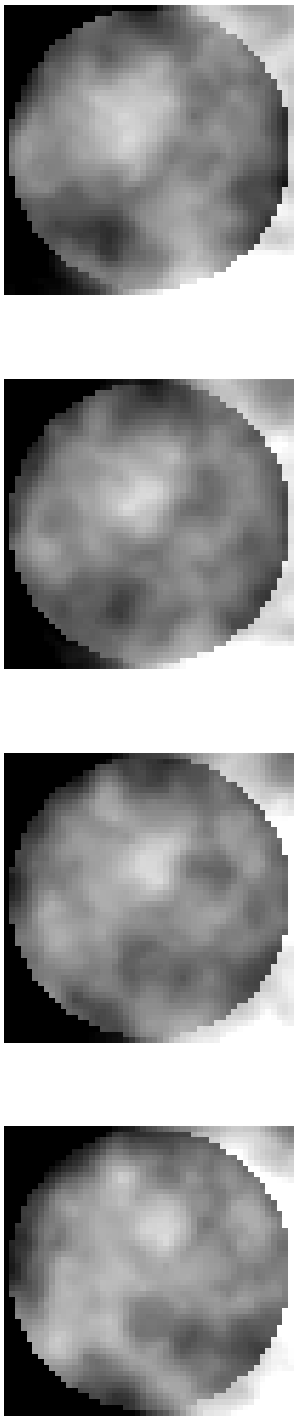

Figure 13: The delay in the wavefront in the AT aperture at four timesteps after the tip and tilt Zernike modes have been corrected.

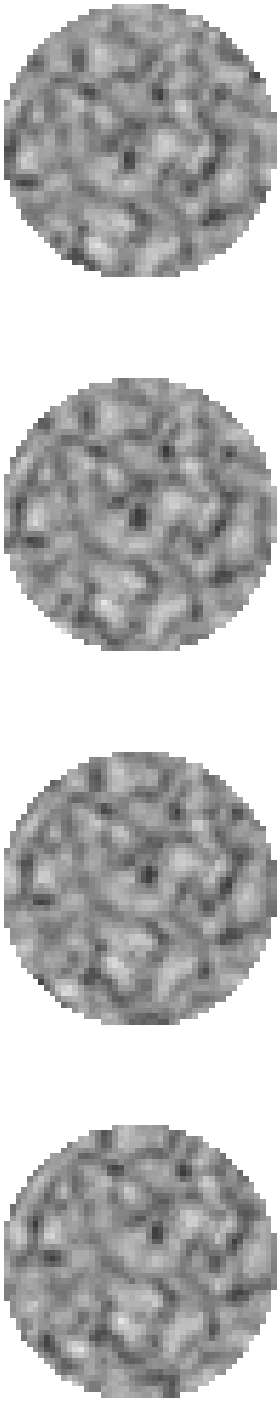

Figure 14: The corresponding optical amplitude in the AT aperture plane.

5 Wavefront corrugations before and after the StS

5.1 Introduction

At several places in the VLTI some form of spatial filtering is performed, whereby the light from certain parts of the image plane is selected to continue along one path through the VLTI, and other light is rejected or sent along a different path. Spatial filtering processes such as this couple the Zernike piston mode to high-order Zernike modes, meaning that the piston mode in the interferometric beam is modulated according to the wavefront corrugations across the aperture plane, as well as modifying the spectral sensitivity distribution (see Section 3.3 for further details of both these effects). As a result, it is necessary to study in detail the expected wavefront corrugations immediately before each VLTI component which performs spatial filtering, which requires numerical simulations of the optical wavefronts at these locations. The first of these components is the StS, which separates the light from one star into two beams when operating in calibration mode. The separation of the beams is done using a roof mirror in the image plane which produces the same effect as a knife-edge test or Schlieren type wavefront detector (see AD 13, 14) in the individual output beams (with each output beam having the knife-edge on the opposite side of the image plane). The amplitude and phase of the output beams are thus strongly (and non-linearly) coupled to the wavefront corrugations in the input beam.

The StS calibration mode relies on both of the output beams from a single star having the same phase. In order investigate the expected performance of this calibration procedure it will be necessary to assess the amount of difference in the wavefront amplitude and phase expected in the two outputs from the StS.

5.2 Dependencies

The wavefront corrugations in the pupil plane immediately before the StS are expected to be closely related to the corrugations found immediately before M1 (see Section 4). The principle difference will be the tip-tilt correction from STRAP, the effects of internal seeing within the AT, vibration of the optical components and the additional optical propagation distance.

5.2.1 This error term is effected by

Error term	Relevant subsection
Wavefront amplitude and phase fluctuations above M1	4.3
Performance of STRAP	G.3
Internal vibration in the VLTI	8.3
Internal seeing within the VLTI	C.3

5.2.2 Error terms effected by this

Error term	Relevant subsection
Wavefront corrugations before VCM	6.3
Atmospheric scintillation and thermal background fluctuations	9.3
Total spectral response of PRIMA system	27.3
Fringe jumps and group tracking errors	28.3

5.3 Detailed contributions

sect:ctb-2-4-3-wavefront-corr-sts

For simulations of the StS calibration mode will be important to accuratly model the dependence of tip-tilt angle on wavelength and on the level of wavefront corrugation across the aperture plane in order to determine the following:

1. The mean and RMS differential phase between the two output channels in StS calibration mode, and the dependence of these parameters on the seeing and the atmospheric refraction and dispersion. This is very complicated, as the phase varies rapidly as a function of position in the image plane both before the StS splitting and in the output beams. Generally each speckle in the image has a arbritary phase between 0 and 2π radians, independent of the other speckles in the image (see Section 3.3 for examples of this).

2. The mean and RMS colour difference between the light leaving the two output channels in StS calibration mode, and the dependence of these parameters on the seeing and the atmospheric refraction and dispersion. Again, the colour of the light varies as a function of position in the image plane of the StS.

Both of these factors depend on the detailed nature of the wavefront corrugation, and thus depend on all the seeing parameters and the STRAP performance.

Although knife-edge or Schlieren wavefront phase detectors are widely used in astronomy (and microscopy), the effect of such a system on the optical phase at the image plane focus is not well documented. The phase perturbations introduced by the atmosphere will be partially converted into amplitude fluctuations in the pupil plane wavefront. Where the amplitude is very low, substantial changes in the wavefront phase may also be observed. In order to assess the impact of the StS roof mirror on interferometric observations, the simulations discussed in Section 3 were modified to include a knife-edge in the image plane. The pupil plane wavefront properties before and after the knife-edge in one timestep from the simulations can be seen in Figures 15 to 20. Figures 15 and 18 show wavefronts entering the StS for this timestep (identical to Figures 9 and 10, although the amplitude is plotted with a different greyscale). The effect of the wavefront corrugations in the input beam on the wavefront amplitude in the output beams is very strong – this is not surprising as the principle use of image plane knife-edges is in visualising wavefront corrugations (see e.g. AD 13, 14). These amplitude fluctuations are much larger than those produced by atmospheric scintillation, and may impede the fringe-tracking performance. Note that the knife-edge also diffracts a significant amount of light out of the beam.

It is clear that detailed simulations will be required in order to determine the expected optical phase and colour differences between the two beams output from the StS when it is operating in calibration mode. As the StS calibration mode represents the fundamental calibration of the PRIMA instrument, it will be important to estimate the phase difference expected between the two output beams in this mode. The two output beams will be swapped periodically using the de-rotator, so it will be important to look for effects which couple the differential phase in the output beams to the angle of the de-rotator.

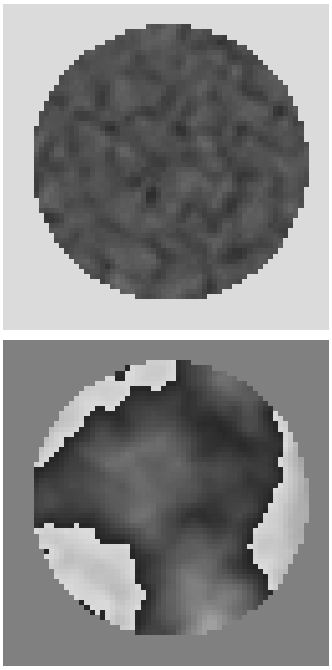

Figure 15: Optical amplitude (upper panel) and phase at 1.97 μm wavelength in the aperture plane before the StS.

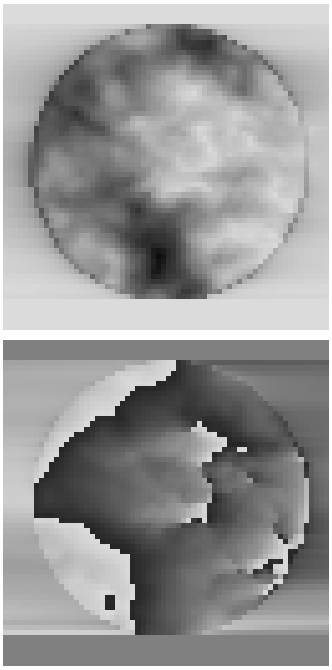

Figure 16: Optical amplitude (upper panel) and phase at 1.97 μm in the aperture plane after an image-plane knife-edge.

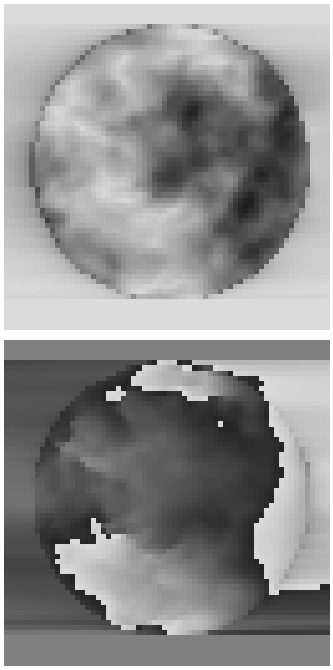

Figure 17: Optical amplitude and phase with the opposite knife-edge (corresponding to the other beam from the StS).

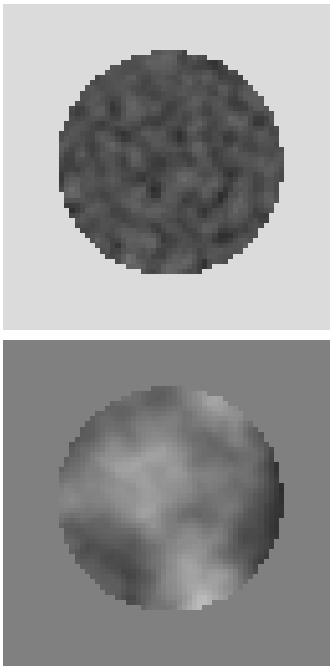

Figure 18: Optical amplitude (upper panel) and phase at 2.43 μm wavelength in the aperture plane before the StS.

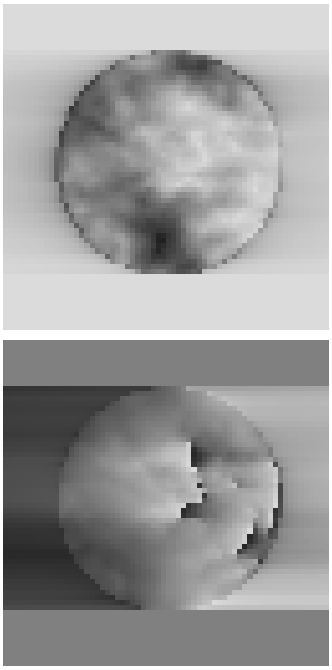

Figure 19: Optical amplitude (upper panel) and phase at 2.43 μm in the aperture plane after an image-plane knife-edge.

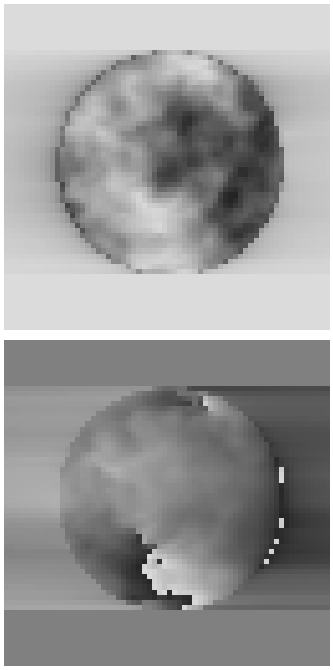

Figure 20: Optical amplitude and phase with the opposite knife-edge (corresponding to the other beam from the StS).

5.4 Impact on astrometry

5.5 Corrective measures required

5.6 Further analysis required

5.7 Conclusion

6 Wavefront corrugations before VCM

6.1 Introduction

The VCMs in the VLTI couple the Zernike piston mode to high-order Zernike modes, meaning that the piston mode in the interferometric beam is modulated according to the wavefront corrugations across the aperture plane. This may cause the astrometric phase to depend on the seeing conditions, the performance of the STRAP units or the effects of vibration. For this reason the wavefront corrugations expected immediately before the VCM will be investigated in detail here.

6.2 Dependencies

6.2.1 This error term is effected by

Error term	Relevant subsection
Wavefront corrugations before and after the StS	5.3
Internal vibration in the VLTI	8.3
Internal seeing within the VLTI	C.3

6.2.2 Error terms effected by this

Error term	Relevant subsection
Wavefront corrugations before FSU spatial filter	7.3
Effect of aberrations in image plane optical components	20.3

6.3 Detailed contributions

sect:ctb-2-4-14-wavefront-corr-vcm

6.4 Impact on astrometry

6.5 Corrective measures required

6.6 Further analysis required

6.7 Conclusion

7 Wavefront corrugations before FSU spatial filter

7.1 Introduction

At several places in the VLTI some form of spatial filtering is performed, whereby the light from certain parts of the image plane is selected to continue along one path through the VLTI, and other light is rejected or sent along a different path. Spatial filtering processes such as this couple the Zernike piston mode to high-order Zernike modes, meaning that the piston mode in the interferometric beam is modulated according to the wavefront corrugations across the aperture plane, as well as modifying the spectral sensitivity distribution (see Section 3.3 for further details of both these effects). As a result, this document will study in detail the expected wavefront corrugations immediately before each VLTI component which performs spatial filtering. The second of these components is the FSU spatial filter, which selects the light from one speckle in the telescope image plane.

Previous studies of the temporal properties of interferometric fringes indicate that the high-frequency fringe motion is dominated by the effects of wavefront corrugations across the aperture plane when the variance in the wavefront phase across the aperture is $\gtrsim 1$ radian. For this reason it will be essential to simulate the level of wavefront corrugation expected in order to determing the performance of the fringe tracker.

7.2 Dependencies

7.2.1 This error term is effected by

Error term	Relevant subsection
Wavefront corrugations before VCM	6.3
Internal vibration in the VLTI	8.3
Internal seeing within the VLTI	C.3

7.2.2 Error terms effected by this

Error term	Relevant subsection
Fringe jumps and group tracking errors	28.3
Total astrometric error	30.3
Systematic errors in the FSU phase	25.3
Atmospheric scintillation and thermal background fluctuations	9.3
Effect of aberrations in image plane optical components	20.3
Total spectral response of PRIMA system	27.3

7.3 Detailed contributions

sect:ctb-2-4-13-wavefront-corr-fsu

7.4 Impact on astrometry

7.5 Corrective measures required

7.6 Further analysis required

7.7 Conclusion

8 Internal vibration in the VLTI

8.1 Introduction

Vibration in optical components in the VLTI will introduce fluctuations in the wavefront phase, particularly in the first three Zernike modes (piston mode and tip-tilt). These may reduce the S/N ratio for fringe tracking. Tip-tilt fluctuations may also result in a systematic error in the measured astrometric phase even if the mean tip and tilt are removed.

8.2 Dependencies

8.2.1 This error term is effected by

Error term	Relevant subsection
Seismic Activity	H.3

8.2.2 Error terms effected by this

Error term	Relevant subsection
Limiting magnitudes for PRIMA	29.3
Fringe jumps and group tracking errors	28.3
Wavefront corrugations before and after the StS	5.3
Wavefront corrugations before VCM	6.3
Wavefront corrugations before FSU spatial filter	7.3

8.3 Detailed contributions

sect:ctb-1-1-5-vibration

8.4 Impact on astrometry

8.5 Corrective measures required

8.6 Further analysis required

8.7 Conclusion

9 Atmospheric scintillation and thermal background fluctuations

9.1 Introduction

9.1.1 Scintillation

Phase perturbations in the wavefronts from a star produce fluctuations in the optical amplitude after the light has propagated down through the atmosphere. The phase measured by the FSU corresponds to an integral of the contributions over both AT pupil planes, and this measurement will naturally be weighted by the amplitude at each point in the pupil plane. In the absence of internal seeing within the VLTI and with accurate pupil relay the scintillation in the pupil plane in front of the FSU will match the scintillation across the AT aperture. However, if there is internal seeing within the VLTI away from the pupil plane additional scintillation can be generated at the FSU. Incorrect pupil relay can also modify the level of scintillation at the FSU.

The simulations described in Section 3 were used to investigate the approximate level of scintillation expected at the telescope aperture. Example plots from 4 timesteps of the simulations were shown in Section 4. Figure 14 shows the optical amplitude as a function of position in the AT aperture plane. It is clear that the amplitude fluctuations are dominated by one of the layers moving from the upper right to the lower left. The dominant layer is the higher one (5 km above the telescope – see Section 3.2).

9.2 Dependencies

9.2.1 This error term is effected by

Error term	Relevant subsection
Wavefront amplitude and phase fluctuations above M1	4.3
Wavefront corrugations before and after the StS	5.3
Wavefront corrugations before FSU	7.3
Ground level temperature, humidity and pressure fluctuations	E.3.2
Air flow through the VLTI	F.3
Thermal load in MDL	B.3.1
Thermal load in laboratory	B.3.2
Drift in image plane VCMs	13.3

9.2.2 Error terms effected by this

Error term	Relevant subsection
Fringe jumps and group tracking errors	28.3
Total spectral response of the PRIMA system	27.3
Limiting magnitudes for PRIMA	29.3
Systematic errors in the FSU phase	25.3

9.3 Detailed contributions

sect:ctb-1-1-4-scintillation

9.3.1 Scintillation

Effect of scintillation

9.3.2 Thermal background fluctuations

Effect of thermal background fluctuations

9.4 Impact on astrometry

9.5 Corrective measures required

9.6 Further analysis required

9.7 Conclusion

10 Effect of detector noise and photon shot noise

10.1 Introduction

Detector noise and photon shot noise are expected to limit the sensitivity of PRIMA observations, but are not expected to introduce significant systematic errors into the astrometric observations. It will be important to have a reasonably realistic model of the detector noise for the PRIMA FSUs. The simulations presented in this document do not take account of detector noise and photon shot noise – it will be important to incorporate these effects in the models of the fringe tracking performance discussed in Section 28.

10.2 Dependencies

10.2.1 This error term is effected by

Error term	Relevant subsection
Observing parameters	N.3

10.2.2 Error terms effected by this

Error term	Relevant subsection
Limiting magnitudes for PRIMA	29.3
Fringe jumps and group tracking errors	28.3
Systematic errors in the FSU phase	25.3

10.3 Detailed contributions

sect:ctb-1-1-3-detector-noise

10.3.1 Effect on S/N ratio for fringe measurements

10.3.2 Effect on astrometric error

10.4 Impact on astrometry

10.5 Corrective measures required

10.6 Further analysis required

10.7 Conclusion

11 Polarisation effects

11.1 Introduction

Murakawa Koji will be studying this component of the error budget in detail.

11.2 Dependencies

11.2.1 This error term is effected by

Error term	Relevant subsection

11.2.2 Error terms effected by this

Error term	Relevant subsection
Systematic errors in the FSU phase	25.3

11.3 Detailed contributions

sect:ctb-2-4-9-polarisation

11.4 Impact on astrometry

11.5 Corrective measures required

11.6 Further analysis required

11.7 Conclusion

12 Refractive index of air and colour of correlated flux

12.1 Introduction

The variation of refractive index with wavelength in the ducts, tunnels and laboratory, and the dependence of the measured astrometric phase on the colour of the correlated flux.

This section will be replaced by text from Richard Mathar

This document gives an order-of-magnitude calculation for the impact of air in the VLTI on differential astrometry. Both the main delay line and differential delay line are assumed to be filled with air. Some error terms are larger per metre air path offset of the DDL than per metre air path offset of the main delay line (notably errors from the uncertainty in the environmental conditions in the VLTI, and uncertainty in empirical/theoretical models for the dispersion in air and water vapour in the near infrared). Other error terms are larger per metre air path offset of the main delay line than per metre air path offset of the DDL (notably errors due to the uncertainty in the stellar wavelength/temperatures).

Errors resulting from the uncertainty in the environmental conditions in the VLTI are found to be negligible, while the errors due to the uncertainty in the stellar temperatures are found to be too large to allow accurate astrometric measurement unless the spectral resolution of PRIMA is enhanced, or a novel method is found for determining the centroid of the correlated flux from each star. There is some disagreement between published models for dispersion in air and water vapour, and until this is resolved it will not be possible to run the DDL without evacuating it. The DDLs could be used for characterising the dispersion of air at near infrared wavelengths. If an alternative method can be found for obtaining laboratory measurements of the refractive index of air and water vapour in the K-band and at the laser metrology wavelength, then it may not be necessary to make the DDLs vacuum-compatible.

The PRIMA facility is intended to measure differential OPD to an accuracy of 5nm in order to allow astrometric detection of the motion of stars due to orbiting planets AD 15, 16. The light from astronomical sources will be passed along air-filled ducts and tunnels in the VLTI, and the primary OPD correction will be performed in an air-filled delay line. In order to calculate the performance of the VLTI it will be necessary to know the refractive index of air in the VLTI in the observing bandpass and at the wavelength of the metrology lasers. Recent studies of the refractive index of air at near infrared wavelengths show notable disagreement, particularly concerning the influence of airbourne water vapour AD 12, 17, 18, 19, 20, 21, and it will be important to resolve this issue before the PRIMA facility is operated. The most established model of refractive index AD 17 has water vapour corrections based on experiments at wavelengths shorter than 0.64 μ m AD 22. Extrapolating these curves to K-band (beyond the near infrared water absorption bands) is scientifically dubious.

If the DDLs can be evacuuated, it may be possible to investigate the refractive index of air and water vapour at near infrared wavelengths using internal calibration light sources at the VLTI. It may be difficult to obtain dispersion measurements of sufficient accuracy using the DDL because of the small stroke length of the DDL.

12.2 Dependencies

12.2.1 This error term is effected by

Error term	Relevant subsection
Model for the refractive index of air	I.3
Total spectral response of PRIMA system	27.3
Knowledge of stellar spectra	26.3
Observing parameters	N.3

12.2.2 Error terms effected by this

Error term	Relevant subsection
Total astrometric error	30.3
Fringe jumps and group tracking errors	28.3

12.3 Detailed contributions

sect:ctb-1-2-1-ref-ind-and-col

If both the main delay line and differential delay line are filled with air, then the measured distances within the VLTI must be converted to OPD at the observing wavelength for each star. The observing wavelength for each star is the centroid of the correlated flux detected for that star. If the observing wavelength of the primary star is λ_{ps}, the observing wavelength of the secondary star is λ_{ses} and the metrology wavelength is λ_m, then the ΔOPD measured at the laser wavelength ΔD_l is given by:

$$\Delta D_l = \frac{(D+\Delta D)\, n_{\lambda_{ses}}}{n_{\lambda_m}} - \frac{D n_{\lambda_{ps}}}{n_{\lambda_m}} \tag{20}$$

$$\Delta D_l \simeq (D+\Delta D)\,(1+n_{\lambda_{ses}}-n_{\lambda_m}) - D\left(1+n_{\lambda_{ps}}-n_{\lambda_m}\right) \tag{21}$$

$$= \Delta D + \Delta D\,(n_{\lambda_{ses}}-n_{\lambda_m}) + D\left(n_{\lambda_{ses}}-n_{\lambda_{ps}}\right) \tag{22}$$

where D is the OPD corrected in the main delay line, and ΔD is the OPD corrected in the DDL. The second term on the right hand side of Equation 22 corresponds to the effect of the air in the DDL, while the third term correponds to the effect of the air in the main delay line. The approximation in Equation 21 is fully valid for this error analysis due to the low refractivity of air.

We wish to measure ΔD:

$$\Delta D = \Delta D_l - \Delta D\,(n_{\lambda_{ses}}-n_{\lambda_m}) - D\left(n_{\lambda_{ses}}-n_{\lambda_{ps}}\right) \tag{23}$$

The conversion from ΔD_l would be done using the best estimates of $n_{\lambda_{ses}}$ and $n_{\lambda_{ps}}$ available. The error $\epsilon(\Delta D)$ in the differential OPD measurement ΔD can be separated into a number of principle terms:

$$\epsilon(\Delta D) = \epsilon(\Delta D_l) + \Delta D\epsilon\,(n_{\lambda_{ses}}-n_{\lambda_m}) - D\epsilon\left(n_{\lambda_{ses}}-n_{\lambda_{ps}}\right) \tag{24}$$

where

$$\epsilon\,(n_{\lambda_{ses}}-n_{\lambda_m}) \tag{25}$$

is the error in estimation of $n_{\lambda_{ses}} - n_{\lambda_m}$,

$$\epsilon\left(n_{\lambda_{ses}} - n_{\lambda_{ps}}\right) \tag{26}$$

is the error in estimation of $n_{\lambda_{ses}} - n_{\lambda_{ps}}$ and

$$\epsilon\left(\Delta D_l\right) \tag{27}$$

is the (hopefully insignificant) error in the ability of the metrology system to count laser wavelengths.

The error terms in Equations 25 and 26 can be further broken down by taking partial derivatives. I will use the following approach:

$$Z = XY \tag{28}$$

$$\Delta Z = \Delta X \frac{\partial\left(XY\right)}{\partial X} + \Delta Y \frac{\partial\left(XY\right)}{\partial Y} \tag{29}$$

Applying this approach to Equation 25 yields:

$$\epsilon\left(n_{\lambda_{ses}} - n_{\lambda_m}\right) = \left\{ \begin{array}{l} \epsilon\left(\rho_a\right) \frac{\partial\left(n_{\lambda_{ses}} - n_{\lambda_m}\right)}{\partial \rho_a} + \epsilon\left(\rho_w\right) \frac{\partial\left(n_{\lambda_{ses}} - n_{\lambda_m}\right)}{\partial \rho_w} \\ + \epsilon\left(\lambda_{ses}\right) \frac{\partial\left(n_{\lambda_{ses}} - n_{\lambda_m}\right)}{\partial \lambda_{ses}} + \epsilon\left(\frac{\Delta\left(n_\lambda\right)}{\Delta\lambda}\right)\left(n_{\lambda_{ses}} - n_{\lambda_m}\right) \end{array} \right. \tag{30}$$

$$\epsilon\left(n_{\lambda_{ses}} - n_{\lambda_{ps}}\right) = \left\{ \begin{array}{l} \epsilon\left(\rho_a\right) \frac{\partial\left(n_{\lambda_{ses}} - n_{\lambda_{ps}}\right)}{\partial \rho_a} + \epsilon\left(\rho_w\right) \frac{\partial\left(n_{\lambda_{ses}} - n_{\lambda_{ps}}\right)}{\partial \rho_w} \\ + \epsilon\left(\lambda_{ses}\right) \frac{\partial\left(n_{\lambda_{ses}} - n_{\lambda_{ps}}\right)}{\partial \lambda_{ses}} + \epsilon\left(\lambda_{ps}\right) \frac{\partial\left(n_{\lambda_{ses}} - n_{\lambda_{ps}}\right)}{\partial \lambda_{ps}} \\ + \epsilon\left(\frac{\Delta\left(n_\lambda\right)}{\Delta\lambda}\right)\left(n_{\lambda_{ses}} - n_{\lambda_{ps}}\right) \end{array} \right. \tag{31}$$

where ρ_a is the air density and ρ_w is the water vapour density in the VLTI. $\epsilon\left(\frac{\Delta\left(n_\lambda\right)}{\Delta\lambda}\right)$ is the uncertainty in the model for dispersion of the air and water vapour in the VLTI between two wavelengths.

Typical values of the components making up these error terms are listed in Table 1.

From Table 1 we can calculate approximate magnitudes for the error terms listed in Equation 30 for the air path in the DDL

$$\epsilon\left(\rho_a\right) \frac{\partial\left(n_{\lambda_{ses}} - n_{\lambda_m}\right)}{\partial \rho_a} \simeq 2 \times 10^{-11} \tag{32}$$

$$\epsilon\left(\rho_w\right) \frac{\partial\left(n_{\lambda_{ses}} - n_{\lambda_m}\right)}{\partial \rho_w} \simeq 5 \times 10^{-12} \tag{33}$$

$$\epsilon\left(\lambda_{ses}\right) \frac{\partial\left(n_{\lambda_{ses}} - n_{\lambda_m}\right)}{\partial \lambda_{ses}} \simeq 8 \times 10^{-10} \tag{34}$$

with an additional term $\epsilon\left(\frac{\Delta\left(n_\lambda\right)}{\Delta\lambda}\right)$ from the dispersive properties of air, which is currently unknown.

If a reliable model for the refractive index of air can be constructed, then it is clear that the error in the colour of the observing band for the secondary star will dominate over the contribution from air in the DDL, giving an total error contribution of (summing errors in quadrature):

$$\epsilon\left(n_{\lambda_{ses}} - n_{\lambda_m}\right) \simeq 8 \times 10^{-10} \tag{35}$$

in units of metres of OPD error per metre air path in the DDL. This corresponds to 0.08 nm error for 10 cm of air path in the DDL.

Table 1: Individual components of the error terms listed in Equation 30

Term	Typical value	Units
$\epsilon\left(\rho_a\right)$	0.005	fractional error
$\frac{\partial(n_{\lambda_{ses}}-n_{\lambda_m})}{\partial\rho_a}$	3×10^{-9}	$\frac{\text{fractional change}}{\text{fractional change}}$
$\frac{\partial\left(n_{\lambda_{ses}}-n_{\lambda_{ps}}\right)}{\partial\rho_a}$	1×10^{-11}	$\frac{\text{fractional change}}{\text{fractional change}}$
$\epsilon\left(\rho_w\right)$	0.0005	fractional error
$\frac{\partial(n_{\lambda_{ses}}-n_{\lambda_m})}{\partial\rho_w}$	1×10^{-8}	$\frac{\text{fractional change}}{\text{fractional change}}$
$\frac{\partial\left(n_{\lambda_{ses}}-n_{\lambda_{ps}}\right)}{\partial\rho_w}$	3×10^{-11}	$\frac{\text{fractional change}}{\text{fractional change}}$
$\epsilon\left(\lambda_{ses}\right)$	2	nm
$\frac{\partial(n_{\lambda_{ses}}-n_{\lambda_m})}{\partial\lambda_{ses}}$	4×10^{-10}	$\frac{\text{fractional change}}{\text{nm}}$
$\frac{\partial\left(n_{\lambda_{ses}}-n_{\lambda_{ps}}\right)}{\partial\lambda_{ses}}$	4×10^{-10}	$\frac{\text{fractional change}}{\text{nm}}$
$\epsilon\left(\lambda_{ps}\right)$	2	nm
$\frac{\partial\left(n_{\lambda_{ses}}-n_{\lambda_{ps}}\right)}{\partial\lambda_{ps}}$	4×10^{-10}	$\frac{\text{fractional change}}{\text{nm}}$
$\epsilon\left(\frac{\Delta(n_\lambda)}{\Delta\lambda}\right)$	Unknown in the near infrared	

Table 2: Error in differential OPD per unit length of air path in the DDL introduced by uncertainties in the observing conditions

Equation number	Description	m ΔOPD per m air
32	The effect of 0.5% uncertainty in the density of the air in the DDL, due to uncertainties in temperature and pressure	2×10^{-11}
33	The effect of 0.2% uncertainty in the density of the water vapour in the DDL, due to uncertainties in relative humidity, temperature and pressure	5×10^{-12}
34	The effect of a 2 nm uncertainty in the centroid wavelength of the correlated flux from secondary star	8×10^{-10}

Equations 32 to 34 are listed alongside a verbal description in Table 2.

From Table 1 we can also calculate approximate magnitudes for the error terms listed in Equation 31 for the air path in the main delay line:

$$\epsilon\left(\rho_a\right) \frac{\partial\left(n_{\lambda_{ses}} - n_{\lambda_{ps}}\right)}{\partial \rho_a} \simeq 1 \times 10^{-13} \tag{36}$$

$$\epsilon\left(\rho_w\right) \frac{\partial\left(n_{\lambda_{ses}} - n_{\lambda_{ps}}\right)}{\partial \rho_w} \simeq 3 \times 10^{-14} \tag{37}$$

$$\epsilon\left(\lambda_{ses}\right) \frac{\partial\left(n_{\lambda_{ses}} - n_{\lambda_{ps}}\right)}{\partial \lambda_{ses}} \simeq 8 \times 10^{-10} \tag{38}$$

$$\epsilon\left(\lambda_{ps}\right) \frac{\partial\left(n_{\lambda_{ses}} - n_{\lambda_{ps}}\right)}{\partial \lambda_{ps}} \simeq 8 \times 10^{-10} \tag{39}$$

with an additional term $\epsilon\left(\frac{\Delta(n_\lambda)}{\Delta\lambda}\right)$ from the dispersive properties of air, which is currently unknown.

If the refractive indices of air and water vapour can be measured with sufficient reliability, it is clear that the error in the colour of the observing band for the primary and secondary stars will dominate the contribution from air in the main delay line, giving a total error contribution of (summing errors in quadrature):

$$\epsilon\left(n_{\lambda_{ses}} - n_{\lambda_{ps}}\right) = \sqrt{2} \times \epsilon\left(n_{\lambda_{ses}} - n_{\lambda_m}\right) \simeq 1 \times 10^{-9} \tag{40}$$

in units of metres of OPD error per metre of air path compensating vacuum path with the main delay lines. This corresponds to 100 nm differential OPD error for 100 m of air path in the main delay line.

Equations 36 to 39 are listed alongside a verbal description in Table 3.

Table 3: Error in differential OPD introduced by uncertainties in the observing conditions per unit length of air path in the main delay lines and AT ducts which is balancing vacuum path (distance of the main delay line from that of equal OPD to the two telescopes)

Equation number	Description	m ΔOPD per m air
36	The effect of 0.5% uncertainty in the density of the air in the main delay line, due to uncertainties in temperature and pressure	1×10^{-12}
37	The effect of 0.2% uncertainty in the density of the water vapour in the main delay line, due to uncertainties in relative humidity, temperature and pressure	3×10^{-14}
38	The effect of a 2 nm uncertainty in the centroid wavelength of the correlated flux from secondary star	8×10^{-10}
39	The effect of a 2 nm uncertainty in the centroid wavelength of the correlated flux from primary star	8×10^{-10}

12.4 Impact on astrometry

12.5 Corrective measures required

12.6 Further analysis required

12.7 Conclusion

Currently the largest uncertainty lies in published models for the refractive index of air and water vapour across the near infrared. If the discrepencies between published results can be resolved (either through a better understanding of errors in previous models of air refractive index, or through new measurements) then it may not be necessary to evacuuate the DDL during PRIMA astrometric operations. The DDLs could be used for characterising the dispersion of air at near infrared wavelengths. If an alternative method is found for obtaining laboratory measurements of the refractive index of air in the K-band and at the laser metrology wavelength before construction of the DDL begins, then it may not be necessary to make the DDLs vacuum-compatible.

If an accurate model for the refractive index is obtained, then an error budget for the effects of air in the VLTI can be constructed. A metre of air path in the main delay line introduces a larger error for differential astrometry measurements than a metre of air introduced in the DDL. The error due to the uncertainty in stellar temperature and stellar spectrum is currently far too large to meet the astrometric accuracy requirements. This error scales as $\frac{1}{R^2}$ for stellar temperature uncertainties where

R is the spectral resolution of PRIMA. A small increase in the spectral resolution of PRIMA should allow accurate astrometry to take place. Alternatively, PRIMA could be operated as a Fourier-transform spectrometer in order to accurately measure the centroid wavelength of the observing bandpass for each astronomical target.

13 Drift in image plane VCMs

13.1 Introduction

The inflated mirrors in the VCMs are expected to show some pressure dependence, which may result in piston, wavefront tilt or pupil re-imaging errors being introduced into the beams. The performance of the VCMs will have to be investigated in detail.

13.2 Dependencies

13.2.1 This error term is effected by

Error term	Relevant subsection
Ground level temperature, humidity and pressure fluctuations	E.3.2

13.2.2 Error terms effected by this

Error term	Relevant subsection
Atmospheric scintillation and thermal background fluctuations	9.3
Total astrometric error	30.3
Effect of aberrations in pupil plane optical components	23.3

13.3 Detailed contributions

sect:ctb-1-2-3-vcm-drift

13.4 Impact on astrometry

13.5 Corrective measures required

13.6 Further analysis required

13.7 Conclusion

14 Variation in VLTI fundamental length calibration

14.1 Introduction

This section deals purely with the metrology laser performance (and not with variations in the refractive index, which are included in Section 12). We have been assured that the drift in the frequency of the laser is negligible, so little work will be required.

14.2 Dependencies

14.2.1 This error term is effected by

Error term	Relevant subsection
Ground level temperature, humidity and pressure fluctuations	E.3.2

14.2.2 Error terms effected by this

Error term	Relevant subsection

14.3 Detailed contributions

sect:ctb-1-2-4-metrology

14.4 Impact on astrometry

14.5 Corrective measures required

14.6 Further analysis required

14.7 Conclusion

15 VLTI baseline geometry

15.1 Introduction

The VLTI baseline geometry is quite complex, as it is defined by the position of M2 as imaged from the sky by M1. Any tilt in M1 results in a substantial movement of the image of M2. The expected baseline error will have to be investigated in some detail.

15.2 Dependencies

15.2.1 This error term is effected by

Error term	Relevant subsection
Ground level temperature, humidity and pressure fluctuations	E.3.2
Total spectral response of PRIMA system	27.3
Knowledge of stellar spectra	26.3
Wavefront amplitude and phase fluctuations above M1	4.3
Earth rotation model	K.3

15.2.2 Error terms effected by this

Error term	Relevant subsection
Total astrometric error	30.3

15.3 Detailed contributions

sect:ctb-1-2-2-baseline-geometry

15.4 Impact on astrometry

15.5 Corrective measures required

15.6 Further analysis required

15.7 Conclusion

16 Systematic differences in baseline length for PS and SeS

16.1 Introduction

Differences in the colour or the elevation of the PS and SeS could in principle introduce a difference in the effective baseline length for the interferometric measurements.

16.2 Dependencies

16.2.1 This error term is effected by

Error term	Relevant subsection
Ground level temperature, humidity and pressure fluctuations	E.3.2
Total spectral response of PRIMA system	27.3
Knowledge of stellar spectra	26.3
Wavefront amplitude and phase fluctuations above M1	4.3

16.2.2 Error terms effected by this

Error term	Relevant subsection
Total astrometric error	30.3

16.3 Detailed contributions

sect:ctb-2-4-5-baseline-length-diff

16.4 Impact on astrometry

16.5 Corrective measures required

16.6 Further analysis required

16.7 Conclusion

17 Galactic effects

17.1 Introduction

Motions of the PS and SeS can introduce complex differential astrometry signals. The effects of perspective acceleration and the Correolis effect (if multiple SeSare used with one PS) will have to be studied in detail.

17.2 Dependencies

17.2.1 This error term is effected by

Error term	Relevant subsection
Position of stars in sky	L.3.1
Angular separation of stars on sky	L.3.2

17.2.2 Error terms effected by this

Error term	Relevant subsection
Total astrometric error	30.3

17.3 Detailed contributions

sect:ctb-2-1-galactic

The galactic effects can be broken down into several contributions to the astrometric error:

1. Perspective acceleration due to proper motion of stars
2. Correolis effect for rotating frame of reference for those targets with two reference stars

17.3.1 Perspective acceleration due to proper motion of stars

Any object having a component of its velocity in the plane of the sky will appear to accelerate or decelerate as the angle towards the object changes.

17.3.2 Correolis effect for rotating frame of reference

This effect only applies when there are two or more reference stars around a target. These two stars define a coordinate frame which will rotate with time, producing an apparent acceleration of the target.

17.4 Impact on astrometry

17.5 Corrective measures required

17.6 Further analysis required

17.7 Conclusion

18 Solar System effects

18.1 Introduction

The velocity of Paranal must be taken into account when performing astrometric observations with PRIMA. Existing Solar System models will be adequate for this. Major planets in the Solar System may impact the observations if targets are selected which are close to these planets on the sky.

18.2 Dependencies

18.2.1 This error term is effected by

Error term	Relevant subsection
Position of stars in sky	L.3.1
Angular separation of stars on sky	L.3.2
Date and time of the observations	M.3

18.2.2 Error terms effected by this

Error term	Relevant subsection
Total astrometric error	30.3

The date and time of the observations determines:

1. The position of the Earth
2. The velocity of the Earth
3. The position of the Sun
4. The position of Jupiter
5. The position of Saturn

18.3 Detailed contributions

sect:ctb-2-2-solar-system

This contribution results from relativistic effects within the Solar System. These relativistic effects on angles are due to the velocity of Earth, and gravitational effects due to the influence of the largest masses in the Solar System.

18.3.1 Velocity of Paranal relative to Solar System centre

Special relativistic effect

18.3.2 Gravitational effect of Sun

General relativistic effect

18.3.3 Gravitational effect of Jupiter

General relativistic effect

18.3.4 Gravitational effect of Saturn

General relativistic effect

18.4 Impact on astrometry

18.5 Corrective measures required

18.6 Further analysis required

18.7 Conclusion

19 Systematic effects from the atmosphere

19.1 Introduction

Large scale gradients could be produced in the atmosphere by the effects of nearby mountains or the Pacific Ocean. These gradients are known to effect conventional astrometric observations, and it will be important to take them into account for the PRIMA narrow angle observations.

19.2 Dependencies

19.2.1 This error term is effected by

Error term	Relevant subsection
Large scale structure in the atmosphere above Paranal	E.3

19.2.2 Error terms effected by this

Error term	Relevant subsection
Total astrometric error	30.3

19.3 Detailed contributions

sect:ctb-2-3-atmosphere

19.3.1 Horizontal air density gradient

Mostly from temperature, but also from pressure

19.3.2 Horizontal water vapour density gradient

From absolute humidity

19.4 Impact on astrometry

19.5 Corrective measures required

19.6 Further analysis required

19.7 Conclusion

20 Effect of aberrations in image plane optical components

20.1 Introduction

Pupil plane is set by AT M2. The specifications for the AT foci are shown in Table 20.1. The distances of the AT mirrors along the optical axis are given in Table 20.1.

Focus	f-ratio	focal length (m)	image scale (μm arcsec^{-1})	Field of view (arcmin)	(mm)
Nasmyth	25.0	45.0	218	8	104.6
Coudé	36.2	65.2	316	2	37.8

Mirror Mirror	Distance from last mirror (mm)	Physical distance from M1 along axis (mm)	Reimaged distance from f/1 image plane (mm)
M1	0.0	0.0	Near pupil plane
M2	2493.4	2493.4	Pupil plane
M3	1793.4	4286.8	Near pupil plane
M4	1450.0	5736.8	8
M5	1630.0	7366.8	Near pupil plane
M6	950.0	8316.8	Pupil plane image
M7	4400.0	12716.8	Near pupil plane
M8	1344.6	14061.4	Near pupil plane
M9[1]	2470.2	16531.6	Near pupil plane

20.2 Dependencies

20.2.1 This error term is effected by

Error term	Relevant subsection
Angular separation of stars on sky	L.3.2
Wavefront amplitude and phase fluctuations above M1	4.3
Wavefront corrugations before and after the StS	5.3
Wavefront corrugations before VCM	6.3
Wavefront corrugations before FSU spatial filter	7.3
Position error between beam footprints in StS calibration mode	22.3

20.2.2 Error terms effected by this

Error term	Relevant subsection
Total astrometric error	30.3

[1] before derotator installed

20.3 Detailed contributions

sect:ctb-1-1-6-image-plane-optics

20.3.1 AT M4 aberrations

M4 is not in an image plane, but is close enough to show a very substantial change in the footprint for off-axis stars. This component comes before the STS, and before the laser metrology corner cube, so systematic error terms cannot be eliminated using the normal calibration procedures. The surface of this mirror must be modelled to *nm* accuracy in order to reach the astrometric accuracy required.

Property	Value
f / ratio	?
Plate scale	~ 0.48 mm arcsec^{-1}
Surface roughness	?
Beam diameter	?

20.3.2 AT star separator aberrations

Star separator has one mirror in an image plane and other mirrors close to the image plane.

Property	Value
f / ratio	?
Plate scale	?
Surface roughness	?

20.3.3 Main delay line VCM aberrations

The VCM is very close to an image plane

Property	Value
f / ratio	?
Plate scale	?
Surface roughness	?
Beam diameter	?

20.3.4 Beam compressor flat

The flat mirror in the beam compressor is very close to an image plane

Property	Value
f / ratio	?
Plate scale	?
Surface roughness	?

20.4 Impact on astrometry

20.5 Corrective measures required

20.6 Further analysis required

20.7 Conclusion

21 Image plane optics in the star separator

21.1 Introduction

The image plane optics in the star separator are particularly important as they play a crucial role in the fundamental calibration of PRIMA. The roof mirror will have to be studied in detail. It may be necessary to map surface errors on this mirror to take acount of the effects of the motion of the SeS and PS.

21.2 Dependencies

21.2.1 This error term is effected by

Error term	Relevant subsection
Wavefront corrugations before and after the StS	5.3

21.2.2 Error terms effected by this

Error term	Relevant subsection
Total astrometric error	30.3

21.3 Detailed contributions

sect:ctb-2-4-1-star-sep-image-plane

21.4 Impact on astrometry

21.5 Corrective measures required

21.6 Further analysis required

21.7 Conclusion

22 Position error between beam footprints in Star Separator calibration mode

22.1 Introduction

The star separator calibration mode represents the fundamental calibration of PRIMA. It will be essential to study the effect of differences in the two output beams on the calibration quality which can be achieved.

22.2 Dependencies

22.2.1 This error term is effected by

Error term	Relevant subsection
Ground level temperature, humidity and pressure fluctuations	E.3.2

22.2.2 Error terms effected by this

Error term	Relevant subsection
Effect of aberrations in pupil plane optical components	23.3

22.3 Detailed contributions

sect:ctb-2-4-2-beam-offset-cal-mode

22.4 Impact on astrometry

22.5 Corrective measures required

22.6 Further analysis required

22.7 Conclusion

23 Effect of aberrations in pupil plane optical components

23.1 Introduction

Pupil plane is set by AT M2. The specifications for the AT foci are shown in Table 23.1. The distances of the AT mirrors along the optical axis are given in Table 23.1.

Focus	f-ratio	focal length (m)	image scale (μm arcsec^{-1})	Field of view (arcmin)	(mm)
Nasmyth	25.0	45.0	218	8	104.6
Coudé	36.2	65.2	316	2	37.8

Mirror Mirror	Distance from last mirror (mm)	Physical distance from M1 along axis (mm)	Reimaged distance from M2 (mm)
M1	0.0	0.0	32586
M2	2493.4	2493.4	0
M3	1793.4	4286.8	$\sim$ 1182300
M4	1450.0	5736.8	Near image plane
M5	1630.0	7366.8	
M6	950.0	8316.8	
M7	4400.0	12716.8	
M8	1344.6	14061.4	
M9[1]	2470.2	16531.6	

23.2 Dependencies

23.2.1 This error term is effected by

Error term	Relevant subsection
Position error between beam footprints in StS calibration mode	22.3
Angle error between beams in StS calibration mode	5.3
Wavefront amplitude and phase fluctuations above M1	4.3
Angular separation of stars on sky	L.3.2
Drift in image plane VCMs	13.3

23.2.2 Error terms effected by this

Error term	Relevant subsection
Total astrometric error	30.3

23.3 Detailed contributions

sect:ctb-1-1-7-pupil-plane-optics

[1] before derotator installed

23.3.1 AT M1 aberrations

sect:ctb-1-1-7-pupil-plane-optics-01

M1 is close to a pupil plane, and the beam wander is relatively small.

Property	Value
Beam diameter	?
Beam walk	? mm arcsec^{-1}
Surface roughness	?
Beam diameter	1800/*mbox mm*

23.3.2 AT M2 aberrations

sect:ctb-1-1-7-pupil-plane-optics-02

M2 is the pupil plane, and the beam wander should be very small.

Property	Value
Beam diameter	?
Beam walk	? mm arcsec^{-1}
Surface roughness	?
Beam diameter	138/*mbox mm*

23.3.3 AT M3 aberrations

sect:ctb-1-1-7-pupil-plane-optics-03

M3 is close to a pupil plane, and the beam wander is relatively small.

Property	Value
Beam diameter	?
Beam walk	? mm arcsec^{-1}
Surface roughness	?
Beam diameter	? /*mbox mm*

23.3.4 AT M5 aberrations

sect:ctb-1-1-7-pupil-plane-optics-05

M5 is close to a pupil plane, and the beam wander is relatively small.

23.3.5 AT M6 aberrations

sect:ctb-1-1-7-pupil-plane-optics-06

M6 is in a reimaged pupil plane, and the beam wander is very small.

23.3.6 AT M7 aberrations

sect:ctb-1-1-7-pupil-plane-optics-07

M7 is close to a pupil plane, and the beam wander is relatively small.

23.3.7 AT M8 aberrations

sect:ctb-1-1-7-pupil-plane-optics-08

M8 is close to a pupil plane, and the beam wander is relatively small.

23.3.8 AT derotator aberrations

sect:ctb-1-1-7-pupil-plane-optics-09

23.3.9 AT window aberrations

sect:ctb-1-1-7-pupil-plane-optics-10

23.3.10 Aberrations in star separator mirrors before image plane

sect:ctb-1-1-7-pupil-plane-optics-11a

23.3.11 Aberrations in star separator mirrors after image plane

sect:ctb-1-1-7-pupil-plane-optics-11c

23.3.12 Aberrations in M12 in MDL tunnel

sect:ctb-1-1-7-pupil-plane-optics-12

23.3.13 Aberrations in M13 in MDL tunnel

sect:ctb-1-1-7-pupil-plane-optics-13

23.3.14 Aberrations in M14 in MDL tunnel

sect:ctb-1-1-7-pupil-plane-optics-14

23.3.15 Aberrations in M16 in MDL tunnel

sect:ctb-1-1-7-pupil-plane-optics-16

23.3.16 Aberrations in pupil plane mirror of beam compressor

sect:ctb-1-1-7-pupil-plane-optics-17

23.3.17 Aberrations in DDL window

sect:ctb-1-1-7-pupil-plane-optics-19

23.3.18 Aberrations in pupil plane mirror of DDL

sect:ctb-1-1-7-pupil-plane-optics-20

Property	Value
Beam diameter	?
Beam walk	? mm arcsec^{-1}
Surface roughness	?
Beam diameter	? /*mbox mm*

23.4 Impact on astrometry

23.5 Corrective measures required

23.6 Further analysis required

23.7 Conclusion

24 Effect of beam walk on optics before the StS

24.1 Introduction

Light from the PS and SeS follows different paths before the StS due to the angular separation of the stars on the sky. Surface errors in these mirrors can thus introduce systematic phase differences in the measurements. This effect cannot be eliminated by beam-switching for the mirrors which come before the de-rotator.

24.2 Dependencies

24.2.1 This error term is effected by

Error term	Relevant subsection
Wavefront amplitude and phase fluctuations above M1	4.3
Wavefront corrugations before and after the StS	5.3

24.2.2 Error terms effected by this

Error term	Relevant subsection
Total astrometric error	30.3

24.3 Detailed contributions

sect:ctb-2-4-4-optics-before-star-sep

24.4 Impact on astrometry

24.5 Corrective measures required

24.6 Further analysis required

24.7 Conclusion

25 Systematic errors in the FSU phase

25.1 Introduction

This section will require a lot of input from the designers and manufacturers of the PRIMA FSUs.

25.2 Dependencies

25.2.1 This error term is effected by

Error term	Relevant subsection
Effect of detector noise and photon shot noise	10.3
Polarisation effects	11.3
Wavefront corrugations before FSU spatial filter	7.3
Atmospheric scintillation and thermal background fluctuations	9.3

25.2.2 Error terms effected by this

Error term	Relevant subsection
Total astrometric error	30.3

25.3 Detailed contributions

sect:ctb-2-4-6-fsu-phase-errors

25.4 Impact on astrometry

25.5 Corrective measures required

25.6 Further analysis required

25.7 Conclusion

26 Knowledge of stellar spectra

26.1 Introduction

If the PS and the SeS have different spectra, the will be offset in position in the night sky due to atmospheric refraction. The optical path length correction applied by the air delay lines will be different for each of the two stars, hence introducing an error into the differential astrometry measurements (note that this error is proportional to the offset of the main delay line from the point where the air paths are equalised). In order to subtract this effect, the spectral energy distribution of the correlated flux from each star will have to be accurately determined.

26.2 Dependencies

26.2.1 This error term is effected by

Error term	Relevant subsection

26.2.2 Error terms effected by this

Error term	Relevant subsection
Refractive index of air and colour of correlated flux	12.3
VLTI baseline geometry	15.3
Systematic differences in baseline length for primary and secondary star	16.3

26.3 Detailed contributions

sect:ctb-2-4-8-stellar-spectra

26.4 Impact on astrometry

26.5 Corrective measures required

26.6 Further analysis required

26.7 Conclusion

27 Total spectral response of PRIMA system

27.1 Introduction

The total spectral response of PRIMA will depend on many factors, including the FSU spectral sensitivity, the mirror reflectivities, and the combined effects of atmospheric refraction and the spatial filtering processes in the FSU and in the StS.

27.2 Dependencies

27.2.1 This error term is effected by

Error term	Relevant subsection
Spectral Response of PRIMA Hardware	J.3
Atmospheric scintillation and thermal background fluctuations	9.3
Wavefront corrugations before and after the StS	5.3
Wavefront corrugations before FSU spatial filter	7.3

27.2.2 Error terms effected by this

Error term	Relevant subsection
Refractive index of air and colour of correlated flux	12.3
VLTI baseline geometry	15.3
Systematic differences in baseline length for primary and secondary star	16.3

27.3 Detailed contributions

sect:ctb-2-4-10-spectral-response-tot

27.4 Impact on astrometry

27.5 Corrective measures required

27.6 Further analysis required

27.7 Conclusion

28 Fringe jumps and group tracking errors

28.1 Introduction

Fringe tracking in an interferometer with large apertures and spatial filters is known to be very challenging. There are three regimes of interest to PRIMA:

1. Observations where the performance is limited by the S/N for active fringe tracking
2. Observations where the performance is limited by the S/N for passive observations of the Ses when the fringes are phase-stabilised using the PS
3. Observations where the performance is limited by the S/N for passive observations of the Ses when the fringes are not phase-stabilised.

Under regime 1 above, the configuration of the VLTI should be optimised to provided maximum S/N ratio on the PS. Under typical Paranal seeing conditions the AT diameter is close to the optimum for fringe tracking S/N with ideal tip-tilt correction – under poorer seeing or poorer tip-tilt correction it may be beneficial to stop down the aperture diameter at the FSU. The results of simple simulations which investigate the performance of the group tracking performance on seeing and aperture diameter are presented in later this section. The added complication for the baseline geometry if the pupil is stopped down may outweigh the benefit in fringe-tracking performance. If the UTs are used there may be a stronger case for stopping down the apertures, particularly if the AO system can be matched to the stopped-down aperture geometry.

Under regime 2 above, the configuration of the VLTI should be optimised to provided maximum S/N ratio on the SeS. As the fringes are phase-stabilised, this simply requires the flux through the spatial filter to be optimised. AD 5 shows that even for simple tip-tilt correction the optimum aperture size can be as large as $6r_0$ for an interferometer with spatial filters, so the AT apertures will never have to be stopped down. It also seems likely that the UT apertures would not need to be stopped down to a smaller diameter if MACAO was used in PRIMA observations.

Regime 3 will require more detailed analysis, although it is expected that the optimum operating conditions will be similar to those for regime 1.

The precise performance of PRIMA will also depend on specific characteristics such as the wavelength separation of the group delay tracking channels, the bandpass of the phase-tracking channel and the performance of the tip-tilt correction. For this reason, numerical simulations which are more PRIMA-specific will be required in order to produce a realistic model of the fringe-tracking performance of PRIMA.

28.2 Dependencies

28.2.1 This error term is effected by

Error term	Relevant subsection
Atmospheric scintillation and thermal background fluctuations	9.3
Wavefront corrugations before and after the StS	5.3
Wavefront corrugations before FSU spatial filter	7.3
Refractive index of air and colour of correlated flux	12.3
Wavefront amplitude and phase fluctuations above M1	4.3
Effect of detector noise and photon shot noise	10.3
Internal vibration in the VLTI	8.3

28.2.2 Error terms effected by this

Error term	Relevant subsection
Limiting magnitudes for PRIMA	29.3
Total astrometric error	30.3

28.3 Detailed contributions

sect:ctb-1-2-5-group-tracking-errors

28.3.1 Simulations of PRIMA operation with the ATs

In order to investigate potential sources of noise in the fringe tracking process, the simulations described in Section 3 were modified to include a simple fringe tracking algorithm. Optical propagation through the VLTI was not modelled – the spatially filtered output from two telescope simulations was simply combined to form an interferometer. In the fringe tracking algorithm, the phases of the seven spectral channels used in the simulation were adjusted so as to subtract the fringe offset measured in the previous timestep (or according to the piston mode if it was the first timestep). The seven channels were then combined to produce the two group delay tracking channels and the one phase tracking channel analogous to the PRIMA FSU spectral channels, as described in Section 3.2. The group delay tracking channels were then used to produce an estimate of the change in group delay, and this was used to find the nearest zero-point in the fringe phase.

One of the first interesting results to come out of these simulations was just how difficult group delay estimation is using the two widely spaced wavelength channels from the PRIMA FSU design, particularly during periods of less-than-ideal seeing. When the stellar images at the telescopes are distorted by wavefront corrugations across the telescope apertures, the phases of the fringes in the group delay tracking channels are also perturbed. This perturbation is different in the two different spectral channels, which produces a substantial error in the calculated group delay. This problem was partially solved by low-pass filtering the group delay measurements, causing perturbations due to the atmosphere to be averaged out over 5—10 time units (where one time unit corresponds to the time taken for each atmospheric layer to move r_0, as discussed in Section 3). The fringe tracking algorithm was then found to perform very well, with fringe jumps detected only every few hundred fringe coherence times. Example plots of the fringe tracking performance are shown in Figures 21

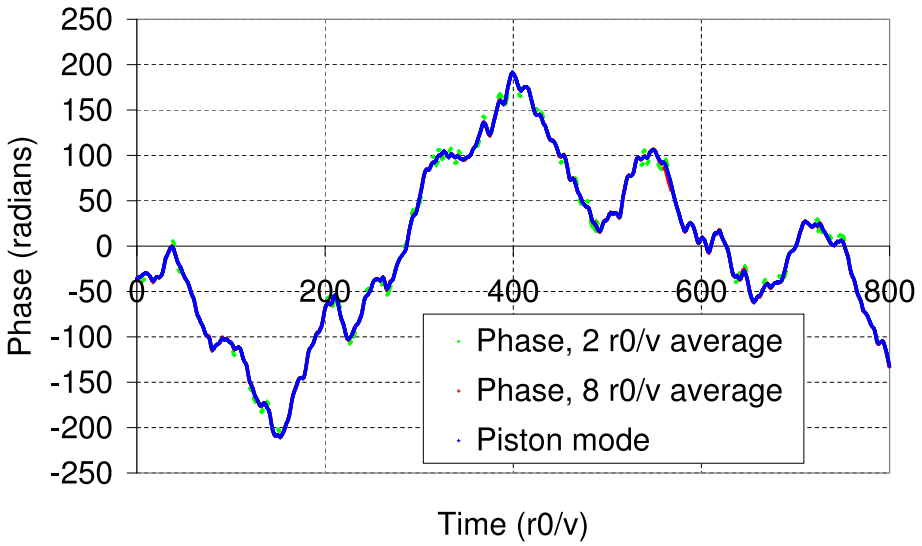

Figure 21: The measured optical phase compared with the piston mode in simulations. The curve labelled *Phase,* $2r_0/v$ *average* shows the optical phase in a simulation where the group delay used in unwrapping the phase is the average group delay over a time period 2 time units ($2r_0/v$). For *Phase,* $8r_0/v$ *average* the averaging is performed over 8 time units. Also shown is the piston mode component. All curves are for the same atmosphere. Photon shot noise and detector noise were not included (the optical phase measurements were noiseless).

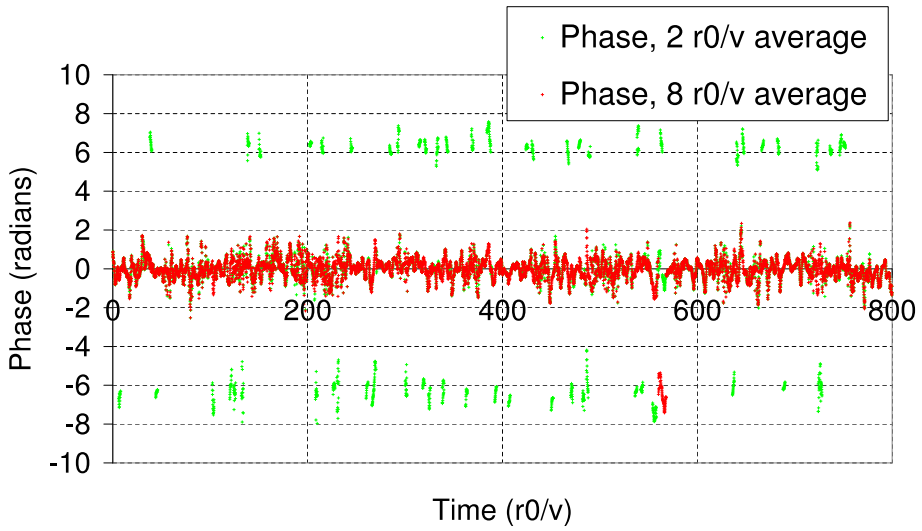

Figure 22: The same data as Figure 21 but the piston mode component has been subtracted from the optical phase data for clarity.

and 22. If the group delay measurements are averaged over too long a period, the algorithm is not able to track the motion of the fringes due to the atmospheric piston mode fluctuations.

These preliminary simulations have also been useful in determining which factors will have the most impact on fringe tracking performance, and hence which should be studied in more detail. Simulations were performed with seeing of $r_0 = 0.45$ m and seeing of $r_0 = 0.9$ m at K band (see Section 2.1 for

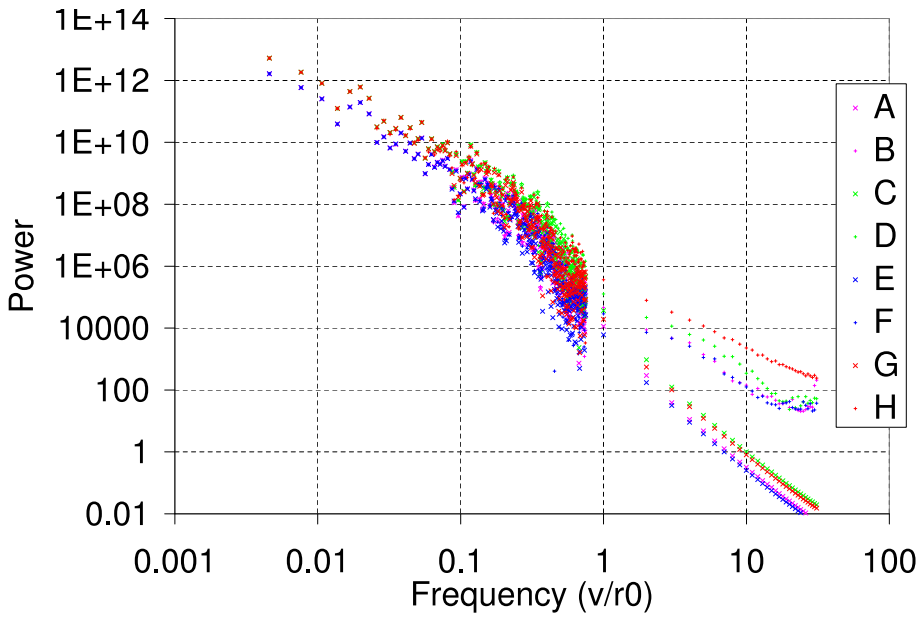

Figure 23: Temporal power spectra of fringe motion. *A* and *B* show the temporal power spectrum of the piston mode and of the fringe phase for simulation 4 (small aperture, good seeing). *C* and *D* show the same for simulation 3 (small aperture, poor seeing). *E* and *F* show the same for simulation 2 (large aperture, good seeing). *G* and *H* show the same for simulation 1 (large aperture, poor seeing). At high frequencies many the datapoints have been binned together and averaged for clarity. The frequency axis is normalised for v/r_0 with the r_0 for the poorer seeing conditions (the Taylor screens moved at the same physical velocity with the good seeing conditions).

an introduction to atmospheric seeing – these numbers correspond approximately to the following two sets of conditions: observing a target at low elevation under below average seeing; and observing a target at the Zenith under excellent seeing). Both the full aperture (1.8 m) and a stopped-down aperture (1.2 m) were simulated. A summary of the simulation characteristics is presented in Table 4. Temporal power spectra of the fringe motion are plotted in Figure 23 for these simulations.

It is clear from the power spectra in Figure 23 that the fringe motion at high frequencies is dominated by the wavefront corrugations across the aperture in all the simulations, and the piston mode component (discussed in e.g. AD 9) is negligible. Note that the piston mode component has a larger high frequency component with smaller aperture sizes as expected, but this is swamped by the effects of wavefront corrugations across the AT aperture, which are much smaller with the smaller aperture size. It is clear that the fringe tracking performance will be determined mostly by the effects of these wavefront corrugations, and that the slow drifts from the piston mode component will be much less important in optimising the fringe tracking algorithm.

The maximum aperture diameter which can successfully used for fringe tracking will be set by the amount of fringe jitter introduced by the wavefront corrugations across the aperture. It is interesting to compare the fringe jitter under different seeing conditions and with different aperture diameters. In this case I have defined the jitter as the residual fringe phase after the piston mode component has been subtracted. There was no photon shot noise or detector noise in these simulations, so this phase difference corresponded directly to the effect of the wavefront corrugations across the aperture plane. A summary of the simulation characteristics and results is presented in Table 5 (the simulations are the same as those presented in Table 4). The likelihood of fringe jumps should be small as long as

Table 4: Simulations of fringe tracking.

	Simulation 1	Simulation 2	Simulation 3	Simulation 4
K band r_0	0.45 m	0.9 m	0.45 m	0.9 m
Seeing* if $Z = 0°$	1.4”	0.68”	1.4”	0.68”
Seeing* if $Z = 60°$	0.89”	0.45”	0.89”	0.45”
Aperture diameter	1.8 m	1.8 m	1.2 m	1.2 m

*500 nm Zenith seeing which would give the appropriate K band r_0 for observations at the Zenith angle Z listed.

Table 5: Phase jitter resulting from wavefront corrugations in the aperture plane.

	Simulation 1	Simulation 2	Simulation 3	Simulation 4
K band r_0	0.45 m	0.9 m	0.45 m	0.9 m
Aperture diameter	1.8 m	1.8 m	1.2 m	1.2 m
RMS phase jitter	0.81 radians	0.31 radians	0.38 radians	0.30 radians

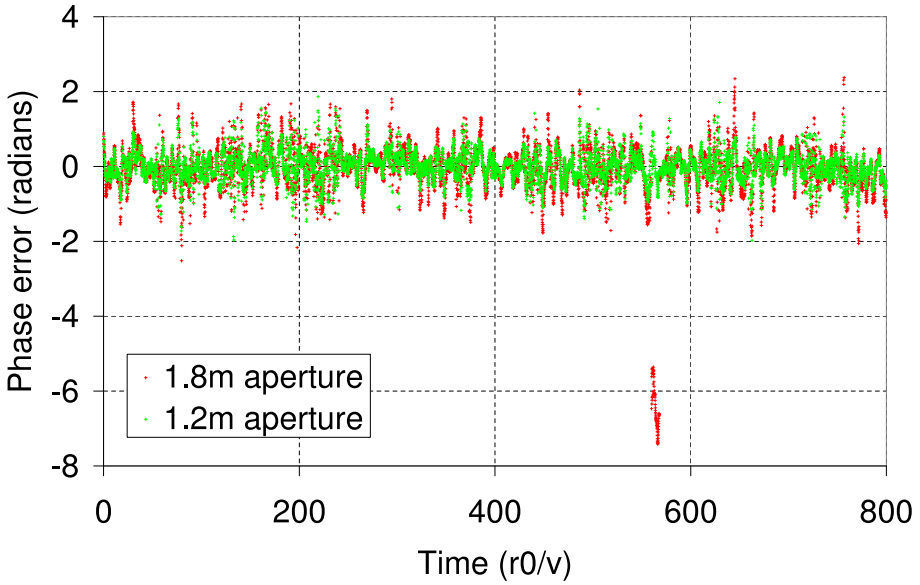

Figure 24: The amount of phase jitter introduced by wavefront corrugations in the aperture plane of an AT. The jitter with the full 1.8 m is shown along with the result when the aperture is stopped-down to 1.2 m diameter. Both simulations used the same atmosphere. Photon shot noise and detector noise were not included (the optical phase measurements were noiseless).

the RMS fringe jitter $\ll 1$ radian.

The phase jitter with the full diameter aperture under the poorer seeing conditions (Simulation 1) is clearly much worse than the other cases. Stopping down the AT aperture provides a very significant reduction in the phase jitter, and appears a promising option at times when fringe tracking becomes very unreliable. Note that the very high phase jitter for Simulation 1 is partly due to a small number of very large phase excursions including fringe jumps, an example of which is shown in Figure 24. Note that the RMS phase jitter is lower for the 1.2 m diameter aperture at all times, however. The loss of stellar flux would make stopping down the telescope aperture less appealing for faint stars.

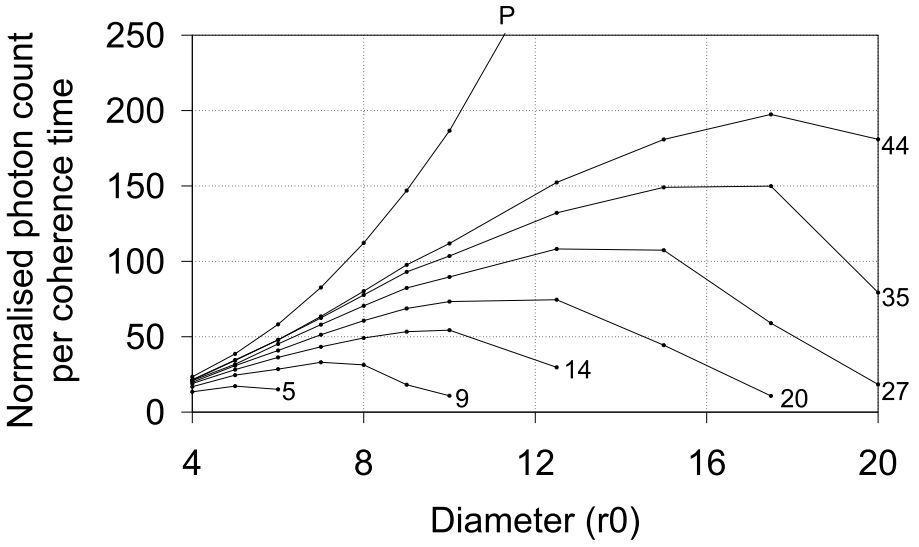

Figure 25: The photon count through a spatial filter per coherence timescale normalised so that a diffraction-limited aperture of diameter r_0 would give unity. The labels on the lines indicate the number of Zernike modes corrected from tip-tilt upwards (describing the level of AO correction). The curve labelled "P" corresponds to the result expected for piston mode only simulations (i.e. with ideal AO correction – see e.g. AD 9). All curves are for the same seeing conditions.

28.3.2 Estimated performance of PRIMA with the UTs

Simulations of PRIMA performance with the UTs have not been undertaken, however some estimates of the probable performance can be made using general properties of optical interferometers. Figure 25 shows the light collected through a spatial filter per coherence time of the interference fringes for a typical interferometer with different levels of AO correction (but all under the same seeing conditions). In this case the AO correction involved ideal compensation of a finite number of Zernike modes (with the modes matched to the aperture diameter used). The decrease in signal for large apertures and low-order AO correction is due to the reduced coherence time for the fringes when the variance in the wavefront phase across the aperture increases beyond 1 radian. It is not clear which (if any) of these curves would correspond to the MACAO system. It is interesting to note that the S/N ratio is optimised when the Strehl ratio is $\sim 30\%$ for all the AO correction models shown here. More realistic simulations of the VLTI would probably be required in order to optimise the operation of PRIMA using the UTs.

28.4 Impact on astrometry

28.5 Corrective measures required

28.6 Further analysis required

28.7 Conclusion

29 Limiting magnitudes for PRIMA

29.1 Introduction

The limiting magnitude of PRIMA will depend critically on the fringe tracking performance, or on the ability to perform passive astrometric measurements without fringe phase tracking.

29.2 Dependencies

29.2.1 This error term is effected by

Error term	Relevant subsection
Wavefront amplitude and phase fluctuations above M1	4.3
Effect of detector noise and photon shot noise	10.3
Atmospheric scintillation and thermal background fluctuations	9.3
Internal vibration in the VLTI	8.3
Fringe jumps and group tracking errors	28.3

29.2.2 Error terms effected by this

Error term	Relevant subsection

29.3 Detailed contributions

sect:ctb-2-4-12-limiting-mag

29.4 Impact on astrometry

29.5 Corrective measures required

29.6 Further analysis required

29.7 Conclusion

30 Total astrometric error

30.1 Introduction

In this section it will be necessary to combine the effects from all the other error terms in this document, and look for inter-dependencies between different error terms.

30.2 Dependencies

30.2.1 This error term is effected by

Error term	Relevant subsection
Effect of aberrations in image plane optical components	20.3
Effect of aberrations in pupil plane optical components	23.3
Refractive index of air and colour of correlated flux	12.3
VLTI baseline geometry	15.3
Drift in image plane VCMs	13.3
Fringe jumps and group tracking errors	28.3
Galactic effects	17.3
Solar System effects	18.3
Systematic effects from the atmosphere	19.3
Wavefront corrugations before FSU spatial filter	7.3
Image plane optics in the star separator	21.3
Effect of beam walk on optics before the Star Separator	24.3
Systematic differences in baseline length for primary and secondary star	16.3
Systematic errors in the FSU phase	25.3

30.2.2 Error terms effected by this

Error term	Relevant subsection

30.3 Detailed contributions

sect:ctb-2-4-11-total-ast-error

30.4 Impact on astrometry

30.5 Corrective measures required

30.6 Further analysis required

30.7 Conclusion

31 Conclusions

General conclusions.

A Temporal and spatial properties of seeing at Paranal

A.1 Introduction

This Appendix will list the general properties of the seeing at Paranal for use in other parts of the error budget.

A.2 Dependencies

A.2.1 This error term is effected by

Error term	Relevant subsection
Wind velocity profile	E.3.1
C_N^2 profile from air density fluctuations	E.3.3
C_N^2 profile from humidity fluctuations	E.3.4
C_N^2 spatial power spectrum and outer scale	E.3.5
C_N^2 spatial and temporal intermittency	E.3.6
Timescale for evolution of turbulence within layers	E.3.7

A.2.2 Error terms effected by this

Error term	Relevant subsection
Wavefront amplitude and phase fluctuations above M1	4.3

A.3 Detailed contributions

sect:ctb-3-1-3-seeing-paranal

A.3.1 Temporal power spectrum of turbulence

A.3.2 Temporal intermittency of seeing

A.4 Impact on astrometry

A.5 Corrective measures required

A.6 Further analysis required

A.7 Conclusion

B Thermal loading in the VLTI

B.1 Introduction

Rudolf Le Poole is currently studying this aspect of the error budget.

B.2 Dependencies

B.2.1 This error term is effected by

Error term	Relevant subsection

B.2.2 Error terms effected by this

Error term	Relevant subsection
Atmospheric scintillation and thermal background fluctuations	9.3
Internal seeing within the VLTI	C.3

B.3 Detailed contributions

sect:ctb-3-1-7-heat-from-vlti

B.3.1 Thermal load in MDL

Contribution from lighting, people etc.

B.3.2 Thermal load in laboratory

Contribution through ceiling, from lighting, people etc.

B.4 Impact on astrometry

B.5 Corrective measures required

B.6 Further analysis required

B.7 Conclusion

C Internal seeing within the VLTI

C.1 Introduction

Text

C.2 Dependencies

C.2.1 This error term is effected by

Error term	Relevant subsection
Ground level temperature, humidity and pressure fluctuations	E.3.2
Air flow through the VLTI	F.3
Thermal load in MDL	B.3.1
Thermal load in laboratory	B.3.2

C.2.2 Error terms effected by this

Error term	Relevant subsection
Wavefront corrugations before FSU spatial filter	7.3
Wavefront corrugations before VCM	6.3
Wavefront corrugations before and after the StS	5.3

C.3 Detailed contributions

sect:ctb-3-1-10-vlti-seeing

C.3.1 Dome seeing

sect:ctb-3-1-10-vlti-seeing-01

C.3.2 AT internal seeing above primary

sect:ctb-3-1-10-vlti-seeing-02

C.3.3 AT internal seeing below secondary

sect:ctb-3-1-10-vlti-seeing-03

C.3.4 AT internal seeing between secondary and STRAP

sect:ctb-3-1-10-vlti-seeing-04

C.3.5 AT internal seeing close to STRAP

sect:ctb-3-1-10-vlti-seeing-05

C.3.6 AT internal seeing between STRAP and derotator

sect:ctb-3-1-10-vlti-seeing-06

C.3.7 AT internal seeing between derotator and AT window

sect:ctb-3-1-10-vlti-seeing-07

C.3.8 AT internal seeing between AT window and STS

sect:ctb-3-1-10-vlti-seeing-08

C.3.9 AT internal seeing close to STS image plane

sect:ctb-3-1-10-vlti-seeing-09

C.3.10 Seeing in AT duct

sect:ctb-3-1-10-vlti-seeing-10

C.3.11 Seeing at interface between AT duct and MDL

sect:ctb-3-1-10-vlti-seeing-11

C.3.12 Seeing in MDL

sect:ctb-3-1-10-vlti-seeing-12

C.3.13 Seeing in MDL carriage

sect:ctb-3-1-10-vlti-seeing-13

C.3.14 Seeing near image plane of MDL carriage

sect:ctb-3-1-10-vlti-seeing-14

C.3.15 Seeing in interface between tunnel and lab

sect:ctb-3-1-10-vlti-seeing-15

C.3.16 Seeing in lab

sect:ctb-3-1-10-vlti-seeing-16

C.3.17 Seeing in beam compressor cats eye

sect:ctb-3-1-10-vlti-seeing-17

C.3.18 Seeing in DDL if air filled

sect:ctb-3-1-10-vlti-seeing-18

C.4 Impact on astrometry

sect:imp-3-1-10-vlti-seeing

C.5 Corrective measures required

sect:cor-3-1-10-vlti-seeing

C.6 Further analysis required

sect:ana-3-1-10-vlti-seeing

C.7 Conclusion

sect:con-3-1-10-vlti-seeing

D Isoplanatism at Paranal

D.1 Introduction

Text

D.2 Dependencies

D.2.1 This error term is effected by

Error term	Relevant subsection
C_N^2 profile from air density fluctuations	E.3.3
C_N^2 profile from humidity fluctuations	E.3.4

D.2.2 Error terms effected by this

Error term	Relevant subsection
Wavefront amplitude and phase fluctuations above M1	4.3

D.3 Detailed contributions

sect:ctb-3-1-2-isoplanatism-paranal

D.4 Impact on astrometry

D.5 Corrective measures required

D.6 Further analysis required

D.7 Conclusion

E Large scale structure in the atmosphere above Paranal

E.1 Introduction

Text

E.2 Dependencies

E.2.1 This error term is effected by

Error term	Relevant subsection

E.2.2 Error terms effected by this

Error term	Relevant subsection
Systematic effects from the atmosphere	19.3
Isoplanatism at Paranal	D.3
Temporal and spatial properties of seeing at Paranal	A.3
Air flow through the VLTI	F.3
Atmospheric scintillation and thermal background fluctuations	9.3
VLTI baseline geometry	15.3
Drift in image plane VCMs	13.3
Variation in VLTI fundamental length calibration	14.3
Position error between beam footprints in Star Separator calibration mode	22.3
Systematic differences in baseline length for primary and secondary star	16.3

E.3 Detailed contributions

sect:ctb-3-1-1-air-density-humidity-profile-paranal

E.3.1 Wind velocity profile

sect:ctb-3-1-1-air-density-humidity-profile-paranal-3

E.3.2 Ground level temperature, humidity and pressure fluctuations

sect:ctb-3-1-1-air-density-humidity-profile-paranal-7

E.3.3 CN-squared profile from air density fluctuations

sect:ctb-3-1-1-air-density-humidity-profile-paranal-1

E.3.4 CN-squared profile from humidity fluctuations

sect:ctb-3-1-1-air-density-humidity-profile-paranal-2

E.3.5 CN-squared power spectrum and outer scale

sect:ctb-3-1-1-air-density-humidity-profile-paranal-4

E.3.6 CN-squared spatial intermittency

sect:ctb-3-1-1-air-density-humidity-profile-paranal-5

E.3.7 Timescale for evolution of turbulence within each layer

sect:ctb-3-1-1-air-density-humidity-profile-paranal-6

E.4 Impact on astrometry

E.5 Corrective measures required

E.6 Further analysis required

E.7 Conclusion

F Air flow through the VLTI

F.1 Introduction

Rudolf Le Poole is currently studying this aspect of the error budget.

F.2 Dependencies

F.2.1 This error term is effected by

Error term	Relevant subsection
Wind velocity profile	E.3.1
Ground level temperature, humidity and pressure fluctuations	E.3.2

F.2.2 Error terms effected by this

Error term	Relevant subsection
Atmospheric scintillation and thermal background fluctuations	9.3
Internal seeing within the VLTI	C.3

F.3 Detailed contributions

sect:ctb-3-1-4-air-flow-through-vlti

F.3.1 Minimising airflow using windows

Possible window materials etc

F.3.2 Minimising airflow without using windows

F.4 Impact on astrometry

F.5 Corrective measures required

F.6 Further analysis required

F.7 Conclusion

G Performance of STRAP

G.1 Introduction

E.g. RMS residual tip-tilt and temporal properties of the tip-tilt errors.

G.2 Dependencies

G.2.1 This error term is effected by

Error term	Relevant subsection
Observing parameters	N.3

G.2.2 Error terms effected by this

Error term	Relevant subsection
Wavefront corrugations before and after the StS	5.3

G.3 Detailed contributions

sect:ctb-3-1-14-strap-performance

G.4 Impact on astrometry

G.5 Corrective measures required

G.6 Further analysis required

G.7 Conclusion

H Seismic Activity

H.1 Introduction

Text

H.2 Dependencies

H.2.1 This error term is effected by

Error term	Relevant subsection

H.2.2 Error terms effected by this

Error term	Relevant subsection
Internal vibration in the VLTI	8.3

H.3 Detailed contributions

sect:ctb-3-1-6-seismic-activity

H.4 Impact on astrometry

H.5 Corrective measures required

H.6 Further analysis required

H.7 Conclusion

I Model for the refractive index of air

I.1 Introduction

Text

I.2 Dependencies

I.2.1 This error term is effected by

Error term	Relevant subsection

I.2.2 Error terms effected by this

Error term	Relevant subsection
Refractive index of air and colour of correlated flux	12.3

I.3 Detailed contributions

sect:ctb-3-1-9-ref-index-model

I.4 Impact on astrometry

I.5 Corrective measures required

I.6 Further analysis required

I.7 Conclusion

J Spectral Response of PRIMA Hardware

J.1 Introduction

Text

J.2 Dependencies

J.2.1 This error term is effected by

Error term	Relevant subsection

J.2.2 Error terms effected by this

Error term	Relevant subsection
Total spectral response of PRIMA system	27.3

J.3 Detailed contributions

sect:ctb-3-1-12-spectral-response-hardw

J.4 Impact on astrometry

J.5 Corrective measures required

J.6 Further analysis required

J.7 Conclusion

K Earth rotation model

K.1 Introduction

Text

K.2 Dependencies

K.2.1 This error term is effected by

Error term	Relevant subsection
Date and time of the observations	M.3

K.2.2 Error terms effected by this

Error term	Relevant subsection
VLTI baseline geometry	15.3

K.3 Detailed contributions

sect:ctb-3-1-11-earth-rotation-model

K.4 Impact on astrometry

K.5 Corrective measures required

K.6 Further analysis required

K.7 Conclusion

L Position and separation of stars

L.1 Introduction

Text

L.2 Dependencies

L.2.1 This error term is effected by

Error term	Relevant subsection

L.2.2 Error terms effected by this

Error term	Relevant subsection
Wavefront amplitude and phase fluctuations above M1	4.3
Effect of aberrations in image plane optical components	20.3
Effect of aberrations in pupil plane optical components	23.3
Galactic effects	17.3
Solar System effects	18.3

L.3 Detailed contributions

sect:ctb-3-1-5-star-separation-angle

L.3.1 Position of stars in sky

L.3.2 Angular separation between stars

L.4 Impact on astrometry

L.5 Corrective measures required

L.6 Further analysis required

L.7 Conclusion

M Date and time of the observations

M.1 Introduction

Text

M.2 Dependencies

M.2.1 This error term is effected by

Error term	Relevant subsection

M.2.2 Error terms effected by this

Error term	Relevant subsection
Solar System effects	18.3
Earth rotation model	K.3

M.3 Detailed contributions

sect:ctb-3-1-8-time-date

M.4 Impact on astrometry

M.5 Corrective measures required

M.6 Further analysis required

M.7 Conclusion

N Observing parameters

N.1 Introduction

E.g. FSU readout rate, aperture diameter used.

N.2 Dependencies

N.2.1 This error term is effected by

Error term	Relevant subsection

N.2.2 Error terms effected by this

Error term	Relevant subsection
Wavefront amplitude and phase fluctuations above M1	4.3
Effect of detector noise and photon shot noise	10.3
Refractive index of air and colour of correlated flux	12.3

N.3 Detailed contributions

sect:ctb-3-1-13-observing-parameters

N.4 Impact on astrometry

N.5 Corrective measures required

N.6 Further analysis required

N.7 Conclusion

O Inter-dependencies

Tables of dependencies for the terms described in this document. Only direct inter-dependencies are listed in Tables 6 and 7, while Tables 8 and 9 include all interdependencies. The tables are include one row per item in the error calculations. For Tables 6 and 8 the right-hand column give the other error terms that the term in this row is dependent on. For Tables 7 and 9 the right-hand column give the other error terms which depend on the term in this row.

At present these dependencies are only available in tabular form, but it is hoped that a graphical description of the dependencies will be produced at a later date.

Term	Section of this document	Other terms this is dependent on (and the appropriate section numbers)
Wavefront amplitude and phase fluctuations above M1	4	Temporal and spatial properties of seeing at Paranal (A), Isoplanatism at Paranal (D), Position and separation of stars (L), Observing parameters (N).
Wavefront corrugations before and after the StS	5	Wavefront amplitude and phase fluctuations above M1 (4), Internal vibration in the VLTI (8), Internal seeing within the VLTI (C). Performance of STRAP (G),
Wavefront corrugations before VCM	6	Wavefront corrugations before and after the StS (5), Internal vibration in the VLTI (8), Internal seeing within the VLTI (C).
Wavefront corrugations before FSU spatial filter	7	Wavefront corrugations before VCM (6), Internal vibration in the VLTI (8), Internal seeing within the VLTI (C).
Internal vibration in the VLTI	8	Seismic Activity (H).
Atmospheric scintillation and thermal background fluctuations	9	Wavefront amplitude and phase fluctuations above M1 (4), Wavefront corrugations before and after the StS (5), Wavefront corrugations before FSU spatial filter (7), Drift in image plane VCMs (13), Thermal loading in the VLTI (B), Large scale structure in the atmosphere above Paranal (E), Air flow through the VLTI (F).
Effect of detector noise and photon shot noise	10	Observing parameters (N).
Refractive index of air and colour of correlated flux	12	Knowledge of stellar spectra (26), Total spectral response of PRIMA system (27), Model for the refractive index of air (I), Observing parameters (N).
Drift in image plane VCMs	13	Large scale structure in the atmosphere above Paranal (E).
Variation in VLTI fundamental length calibration	14	Large scale structure in the atmosphere above Paranal (E).

VLTI baseline geometry	15	Wavefront amplitude and phase fluctuations above M1 (4), Knowledge of stellar spectra (26), Total spectral response of PRIMA system (27), Large scale structure in the atmosphere above Paranal (E), Earth rotation model (K).
Systematic differences in baseline length for primary and secondary star	16	Wavefront amplitude and phase fluctuations above M1 (4), Knowledge of stellar spectra (26), Total spectral response of PRIMA system (27), Large scale structure in the atmosphere above Paranal (E).
Galactic effects	17	Position and separation of stars (L).
Solar System effects	18	Position and separation of stars (L), Date and time of the observations (M).
Systematic effects from the atmosphere	19	Large scale structure in the atmosphere above Paranal (E).
Effect of aberrations in image plane optical components	20	Wavefront amplitude and phase fluctuations above M1 (4), Wavefront corrugations before and after the StS (5), Wavefront corrugations before VCM (6), Wavefront corrugations before FSU spatial filter (7), Position error between beam footprints in Star Separator calibration mode (22), Position and separation of stars (L).
Image plane optics in the star separator	21	Wavefront corrugations before and after the StS (5).
Position error between beam footprints in Star Separator calibration mode	22	Large scale structure in the atmosphere above Paranal (E).
Effect of aberrations in pupil plane optical components	23	Wavefront amplitude and phase fluctuations above M1 (4), Wavefront corrugations before and after the StS (5), Drift in image plane VCMs (13), Position error between beam footprints in Star Separator calibration mode (22), Position and separation of stars (L).
Effect of beam walk on optics before the Star Separator	24	Wavefront amplitude and phase fluctuations above M1 (4), Wavefront corrugations before and after the StS (5).
Systematic errors in the FSU phase	25	Wavefront corrugations before FSU spatial filter (7), Atmospheric scintillation and thermal background fluctuations (9), Effect of detector noise and photon shot noise (10), Polarisation effects (11).
Total spectral response of PRIMA system	27	Wavefront corrugations before and after the StS (5), Wavefront corrugations before FSU spatial filter (7), Atmospheric scintillation and thermal background fluctuations (9), Spectral Response of PRIMA Hardware (J).

Fringe jumps and group tracking errors	28	Wavefront amplitude and phase fluctuations above M1 (4), Wavefront corrugations before and after the StS (5), Wavefront corrugations before FSU spatial filter (7), Internal vibration in the VLTI (8), Atmospheric scintillation and thermal background fluctuations (9), Effect of detector noise and photon shot noise (10), Refractive index of air and colour of correlated flux (12).
Limiting magnitudes for PRIMA	29	Wavefront amplitude and phase fluctuations above M1 (4), Internal vibration in the VLTI (8), Atmospheric scintillation and thermal background fluctuations (9), Effect of detector noise and photon shot noise (10), Fringe jumps and group tracking errors (28).
Total astrometric error	30	Wavefront corrugations before FSU spatial filter (7), Refractive index of air and colour of correlated flux (12), Drift in image plane VCMs (13), VLTI baseline geometry (15), Systematic differences in baseline length for primary and secondary star (16), Galactic effects (17), Solar System effects (18), Systematic effects from the atmosphere (19), Effect of aberrations in image plane optical components (20), Image plane optics in the star separator (21), Effect of aberrations in pupil plane optical components (23), Effect of beam walk on optics before the Star Separator (24), Systematic errors in the FSU phase (25), Fringe jumps and group tracking errors (28).
Temporal and spatial properties of seeing at Paranal	A	Large scale structure in the atmosphere above Paranal (E).
Internal seeing within the VLTI	C	Thermal loading in the VLTI (B), Air flow through the VLTI (F).
Isoplanatism at Paranal	D	Large scale structure in the atmosphere above Paranal (E).
Air flow through the VLTI	F	Large scale structure in the atmosphere above Paranal (E).
Performance of STRAP	G	Observing parameters (N).
Earth rotation model	K	Date and time of the observations (M).

Table 6: Table including only direct dependencies of each error term.

Term	Section of this document	Other terms directly dependent on this (and the appropriate section numbers)
Wavefront amplitude and phase fluctuations above M1	4	Wavefront corrugations before and after the StS (5), Atmospheric scintillation and thermal background fluctuations (9), VLTI baseline geometry (15), Systematic differences in baseline length for primary and secondary star (16), Effect of aberrations in image plane optical components (20), Effect of aberrations in pupil plane optical components (23), Effect of beam walk on optics before the Star Separator (24), Fringe jumps and group tracking errors (28), Limiting magnitudes for PRIMA (29).
Wavefront corrugations before and after the StS	5	Wavefront corrugations before VCM (6), Atmospheric scintillation and thermal background fluctuations (9), Effect of aberrations in image plane optical components (20), Image plane optics in the star separator (21), Effect of aberrations in pupil plane optical components (23), Effect of beam walk on optics before the Star Separator (24), Total spectral response of PRIMA system (27), Fringe jumps and group tracking errors (28).
Wavefront corrugations before VCM	6	Wavefront corrugations before FSU spatial filter (7), Effect of aberrations in image plane optical components (20).
Wavefront corrugations before FSU spatial filter	7	Atmospheric scintillation and thermal background fluctuations (9), Effect of aberrations in image plane optical components (20), Systematic errors in the FSU phase (25), Total spectral response of PRIMA system (27), Fringe jumps and group tracking errors (28), Total astrometric error (30).
Internal vibration in the VLTI	8	Wavefront corrugations before and after the StS (5), Wavefront corrugations before VCM (6), Wavefront corrugations before FSU spatial filter (7), Fringe jumps and group tracking errors (28), Limiting magnitudes for PRIMA (29).
Atmospheric scintillation and thermal background fluctuations	9	Systematic errors in the FSU phase (25), Total spectral response of PRIMA system (27), Fringe jumps and group tracking errors (28), Limiting magnitudes for PRIMA (29).
Effect of detector noise and photon shot noise	10	Systematic errors in the FSU phase (25), Fringe jumps and group tracking errors (28), Limiting magnitudes for PRIMA (29).
Polarisation effects	11	Systematic errors in the FSU phase (25).

Refractive index of air and colour of correlated flux	12	Fringe jumps and group tracking errors (28), Total astrometric error (30).
Drift in image plane VCMs	13	Atmospheric scintillation and thermal background fluctuations (9), Effect of aberrations in pupil plane optical components (23), Total astrometric error (30).
VLTI baseline geometry	15	Total astrometric error (30).
Systematic differences in baseline length for primary and secondary star	16	Total astrometric error (30).
Galactic effects	17	Total astrometric error (30).
Solar System effects	18	Total astrometric error (30).
Systematic effects from the atmosphere	19	Total astrometric error (30).
Effect of aberrations in image plane optical components	20	Total astrometric error (30).
Image plane optics in the star separator	21	Total astrometric error (30).
Position error between beam footprints in Star Separator calibration mode	22	Effect of aberrations in image plane optical components (20), Effect of aberrations in pupil plane optical components (23).
Effect of aberrations in pupil plane optical components	23	Total astrometric error (30).
Effect of beam walk on optics before the Star Separator	24	Total astrometric error (30).
Systematic errors in the FSU phase	25	Total astrometric error (30).
Knowledge of stellar spectra	26	Refractive index of air and colour of correlated flux (12), VLTI baseline geometry (15), Systematic differences in baseline length for primary and secondary star (16).
Total spectral response of PRIMA system	27	Refractive index of air and colour of correlated flux (12), VLTI baseline geometry (15), Systematic differences in baseline length for primary and secondary star (16).
Fringe jumps and group tracking errors	28	Limiting magnitudes for PRIMA (29), Total astrometric error (30).
Temporal and spatial properties of seeing at Paranal	A	Wavefront amplitude and phase fluctuations above M1 (4).

Thermal loading in the VLTI	B	Atmospheric scintillation and thermal background fluctuations (9), Internal seeing within the VLTI (C).
Internal seeing within the VLTI	C	Wavefront corrugations before and after the StS (5), Wavefront corrugations before VCM (6), Wavefront corrugations before FSU spatial filter (7).
Isoplanatism at Paranal	D	Wavefront amplitude and phase fluctuations above M1 (4).
Large scale structure in the atmosphere above Paranal	E	Atmospheric scintillation and thermal background fluctuations (9), Drift in image plane VCMs (13), Variation in VLTI fundamental length calibration (14), VLTI baseline geometry (15), Systematic differences in baseline length for primary and secondary star (16), Systematic effects from the atmosphere (19), Position error between beam footprints in Star Separator calibration mode (22), Temporal and spatial properties of seeing at Paranal (A), Isoplanatism at Paranal (D), Air flow through the VLTI (F).
Air flow through the VLTI	F	Atmospheric scintillation and thermal background fluctuations (9), Internal seeing within the VLTI (C).
Performance of STRAP	G	Wavefront corrugations before and after the StS (5).
Seismic Activity	H	Internal vibration in the VLTI (8).
Model for the refractive index of air	I	Refractive index of air and colour of correlated flux (12).
Spectral Response of PRIMA Hardware	J	Total spectral response of PRIMA system (27).
Earth rotation model	K	VLTI baseline geometry (15).
Position and separation of stars	L	Wavefront amplitude and phase fluctuations above M1 (4), Galactic effects (17), Solar System effects (18), Effect of aberrations in image plane optical components (20), Effect of aberrations in pupil plane optical components (23).
Date and time of the observations	M	Solar System effects (18), Earth rotation model (K).
Observing parameters	N	Wavefront amplitude and phase fluctuations above M1 (4), Effect of detector noise and photon shot noise (10), Refractive index of air and colour of correlated flux (12), Performance of STRAP (G).

Table 7: Table including only direct dependencies of each error term.

Term	Section of this document	Terms this is directly or indirectly dependent on (and the appropriate section numbers)
Wavefront amplitude and phase fluctuations above M1	4	Temporal and spatial properties of seeing at Paranal (A), Isoplanatism at Paranal (D), Large scale structure in the atmosphere above Paranal (E), Position and separation of stars (L), Observing parameters (N).
Wavefront corrugations before and after the StS	5	Wavefront amplitude and phase fluctuations above M1 (4), Internal vibration in the VLTI (8), Temporal and spatial properties of seeing at Paranal (A), Thermal loading in the VLTI (B), Internal seeing within the VLTI (C), Isoplanatism at Paranal (D), Large scale structure in the atmosphere above Paranal (E), Air flow through the VLTI (F), Performance of STRAP (G), Wavefront corrugations before and after the StS (5).
Seismic Activity (H), Position and separation of stars (L), Observing parameters (N).		
Wavefront corrugations before VCM	6	Wavefront amplitude and phase fluctuations above M1 (4), Wavefront corrugations before and after the StS (5), Internal vibration in the VLTI (8), Temporal and spatial properties of seeing at Paranal (A), Thermal loading in the VLTI (B), Internal seeing within the VLTI (C), Isoplanatism at Paranal (D), Large scale structure in the atmosphere above Paranal (E), Air flow through the VLTI (F), Performance of STRAP (G), Seismic Activity (H), Position and separation of stars (L), Observing parameters (N).
Wavefront corrugations before FSU spatial filter	7	Wavefront amplitude and phase fluctuations above M1 (4), Wavefront corrugations before and after the StS (5), Wavefront corrugations before VCM (6), Internal vibration in the VLTI (8), Temporal and spatial properties of seeing at Paranal (A), Thermal loading in the VLTI (B), Internal seeing within the VLTI (C), Isoplanatism at Paranal (D), Large scale structure in the atmosphere above Paranal (E), Air flow through the VLTI (F), Performance of STRAP (G), Seismic Activity (H), Position and separation of stars (L), Observing parameters (N).
Internal vibration in the VLTI	8	Seismic Activity (H).

Atmospheric scintillation and thermal background fluctuations	9	Wavefront amplitude and phase fluctuations above M1 (4), Wavefront corrugations before and after the StS (5), Wavefront corrugations before VCM (6), Wavefront corrugations before FSU spatial filter (7), Internal vibration in the VLTI (8), Drift in image plane VCMs (13), Temporal and spatial properties of seeing at Paranal (A), Thermal loading in the VLTI (B), Internal seeing within the VLTI (C), Isoplanatism at Paranal (D), Large scale structure in the atmosphere above Paranal (E), Air flow through the VLTI (F), Performance of STRAP (G), Seismic Activity (H), Position and separation of stars (L), Observing parameters (N).
Effect of detector noise and photon shot noise	10	Observing parameters (N).
Refractive index of air and colour of correlated flux	12	Wavefront amplitude and phase fluctuations above M1 (4), Wavefront corrugations before and after the StS (5), Wavefront corrugations before VCM (6), Wavefront corrugations before FSU spatial filter (7), Internal vibration in the VLTI (8), Atmospheric scintillation and thermal background fluctuations (9), Drift in image plane VCMs (13), Knowledge of stellar spectra (26), Total spectral response of PRIMA system (27), Temporal and spatial properties of seeing at Paranal (A), Thermal loading in the VLTI (B), Internal seeing within the VLTI (C), Isoplanatism at Paranal (D), Large scale structure in the atmosphere above Paranal (E), Air flow through the VLTI (F), Performance of STRAP (G), Seismic Activity (H), Model for the refractive index of air (I), Spectral Response of PRIMA Hardware (J), Position and separation of stars (L), Observing parameters (N).
Drift in image plane VCMs	13	Large scale structure in the atmosphere above Paranal (E).
Variation in VLTI fundamental length calibration	14	Large scale structure in the atmosphere above Paranal (E).

VLTI baseline geometry	15	Wavefront amplitude and phase fluctuations above M1 (4), Wavefront corrugations before and after the StS (5), Wavefront corrugations before VCM (6), Wavefront corrugations before FSU spatial filter (7), Internal vibration in the VLTI (8), Atmospheric scintillation and thermal background fluctuations (9), Drift in image plane VCMs (13), Knowledge of stellar spectra (26), Total spectral response of PRIMA system (27), Temporal and spatial properties of seeing at Paranal (A), Thermal loading in the VLTI (B), Internal seeing within the VLTI (C), Isoplanatism at Paranal (D), Large scale structure in the atmosphere above Paranal (E), Air flow through the VLTI (F), Performance of STRAP (G), Seismic Activity (H), Spectral Response of PRIMA Hardware (J), Earth rotation model (K), Position and separation of stars (L), Date and time of the observations (M), Observing parameters (N).
Systematic differences in baseline length for primary and secondary star	16	Wavefront amplitude and phase fluctuations above M1 (4), Wavefront corrugations before and after the StS (5), Wavefront corrugations before VCM (6), Wavefront corrugations before FSU spatial filter (7), Internal vibration in the VLTI (8), Atmospheric scintillation and thermal background fluctuations (9), Drift in image plane VCMs (13), Knowledge of stellar spectra (26), Total spectral response of PRIMA system (27), Temporal and spatial properties of seeing at Paranal (A), Thermal loading in the VLTI (B), Internal seeing within the VLTI (C), Isoplanatism at Paranal (D), Large scale structure in the atmosphere above Paranal (E), Air flow through the VLTI (F), Performance of STRAP (G), Seismic Activity (H), Spectral Response of PRIMA Hardware (J), Position and separation of stars (L), Observing parameters (N).
Galactic effects	17	Position and separation of stars (L).
Solar System effects	18	Position and separation of stars (L), Date and time of the observations (M).
Systematic effects from the atmosphere	19	Large scale structure in the atmosphere above Paranal (E).

Effect of aberrations in image plane optical components	20	Wavefront amplitude and phase fluctuations above M1 (4), Wavefront corrugations before and after the StS (5), Wavefront corrugations before VCM (6), Wavefront corrugations before FSU spatial filter (7), Internal vibration in the VLTI (8), Position error between beam footprints in Star Separator calibration mode (22), Temporal and spatial properties of seeing at Paranal (A), Thermal loading in the VLTI (B), Internal seeing within the VLTI (C), Isoplanatism at Paranal (D), Large scale structure in the atmosphere above Paranal (E), Air flow through the VLTI (F), Performance of STRAP (G), Seismic Activity (H), Position and separation of stars (L), Observing parameters (N).
Image plane optics in the star separator	21	Wavefront amplitude and phase fluctuations above M1 (4), Wavefront corrugations before and after the StS (5), Internal vibration in the VLTI (8), Temporal and spatial properties of seeing at Paranal (A), Thermal loading in the VLTI (B), Internal seeing within the VLTI (C), Isoplanatism at Paranal (D), Large scale structure in the atmosphere above Paranal (E), Air flow through the VLTI (F), Performance of STRAP (G), Seismic Activity (H), Position and separation of stars (L), Observing parameters (N).
Position error between beam footprints in Star Separator calibration mode	22	Large scale structure in the atmosphere above Paranal (E).
Effect of aberrations in pupil plane optical components	23	Wavefront amplitude and phase fluctuations above M1 (4), Wavefront corrugations before and after the StS (5), Internal vibration in the VLTI (8), Drift in image plane VCMs (13), Position error between beam footprints in Star Separator calibration mode (22), Temporal and spatial properties of seeing at Paranal (A), Thermal loading in the VLTI (B), Internal seeing within the VLTI (C), Isoplanatism at Paranal (D), Large scale structure in the atmosphere above Paranal (E), Air flow through the VLTI (F), Performance of STRAP (G), Seismic Activity (H), Position and separation of stars (L), Observing parameters (N).

Effect of beam walk on optics before the Star Separator	24	Wavefront amplitude and phase fluctuations above M1 (4), Wavefront corrugations before and after the StS (5), Internal vibration in the VLTI (8), Temporal and spatial properties of seeing at Paranal (A), Thermal loading in the VLTI (B), Internal seeing within the VLTI (C), Isoplanatism at Paranal (D), Large scale structure in the atmosphere above Paranal (E), Air flow through the VLTI (F), Performance of STRAP (G), Seismic Activity (H), Position and separation of stars (L), Observing parameters (N).
Systematic errors in the FSU phase	25	Wavefront amplitude and phase fluctuations above M1 (4), Wavefront corrugations before and after the StS (5), Wavefront corrugations before VCM (6), Wavefront corrugations before FSU spatial filter (7), Internal vibration in the VLTI (8), Atmospheric scintillation and thermal background fluctuations (9), Effect of detector noise and photon shot noise (10), Polarisation effects (11), Drift in image plane VCMs (13), Temporal and spatial properties of seeing at Paranal (A), Thermal loading in the VLTI (B), Internal seeing within the VLTI (C), Isoplanatism at Paranal (D), Large scale structure in the atmosphere above Paranal (E), Air flow through the VLTI (F), Performance of STRAP (G), Seismic Activity (H), Position and separation of stars (L), Observing parameters (N).
Total spectral response of PRIMA system	27	Wavefront amplitude and phase fluctuations above M1 (4), Wavefront corrugations before and after the StS (5), Wavefront corrugations before VCM (6), Wavefront corrugations before FSU spatial filter (7), Internal vibration in the VLTI (8), Atmospheric scintillation and thermal background fluctuations (9), Drift in image plane VCMs (13), Temporal and spatial properties of seeing at Paranal (A), Thermal loading in the VLTI (B), Internal seeing within the VLTI (C), Isoplanatism at Paranal (D), Large scale structure in the atmosphere above Paranal (E), Air flow through the VLTI (F), Performance of STRAP (G), Seismic Activity (H), Spectral Response of PRIMA Hardware (J), Position and separation of stars (L), Observing parameters (N).

Fringe jumps and group tracking errors	28	Wavefront amplitude and phase fluctuations above M1 (4), Wavefront corrugations before and after the StS (5), Wavefront corrugations before VCM (6), Wavefront corrugations before FSU spatial filter (7), Internal vibration in the VLTI (8), Atmospheric scintillation and thermal background fluctuations (9), Effect of detector noise and photon shot noise (10), Refractive index of air and colour of correlated flux (12), Drift in image plane VCMs (13), Knowledge of stellar spectra (26), Total spectral response of PRIMA system (27), Temporal and spatial properties of seeing at Paranal (A), Thermal loading in the VLTI (B), Internal seeing within the VLTI (C), Isoplanatism at Paranal (D), Large scale structure in the atmosphere above Paranal (E), Air flow through the VLTI (F), Performance of STRAP (G), Seismic Activity (H), Model for the refractive index of air (I), Spectral Response of PRIMA Hardware (J), Position and separation of stars (L), Observing parameters (N).
Limiting magnitudes for PRIMA	29	Wavefront amplitude and phase fluctuations above M1 (4), Wavefront corrugations before and after the StS (5), Wavefront corrugations before VCM (6), Wavefront corrugations before FSU spatial filter (7), Internal vibration in the VLTI (8), Atmospheric scintillation and thermal background fluctuations (9), Effect of detector noise and photon shot noise (10), Refractive index of air and colour of correlated flux (12), Drift in image plane VCMs (13), Knowledge of stellar spectra (26), Total spectral response of PRIMA system (27), Fringe jumps and group tracking errors (28), Temporal and spatial properties of seeing at Paranal (A), Thermal loading in the VLTI (B), Internal seeing within the VLTI (C), Isoplanatism at Paranal (D), Large scale structure in the atmosphere above Paranal (E), Air flow through the VLTI (F), Performance of STRAP (G), Seismic Activity (H), Model for the refractive index of air (I), Spectral Response of PRIMA Hardware (J), Position and separation of stars (L), Observing parameters (N).

Total astrometric error	30	Wavefront amplitude and phase fluctuations above M1 (4), Wavefront corrugations before and after the StS (5), Wavefront corrugations before VCM (6), Wavefront corrugations before FSU spatial filter (7), Internal vibration in the VLTI (8), Atmospheric scintillation and thermal background fluctuations (9), Effect of detector noise and photon shot noise (10), Polarisation effects (11), Refractive index of air and colour of correlated flux (12), Drift in image plane VCMs (13), VLTI baseline geometry (15), Systematic differences in baseline length for primary and secondary star (16), Galactic effects (17), Solar System effects (18), Systematic effects from the atmosphere (19), Effect of aberrations in image plane optical components (20), Image plane optics in the star separator (21), Position error between beam footprints in Star Separator calibration mode (22), Effect of aberrations in pupil plane optical components (23), Effect of beam walk on optics before the Star Separator (24), Systematic errors in the FSU phase (25), Knowledge of stellar spectra (26), Total spectral response of PRIMA system (27), Fringe jumps and group tracking errors (28), Temporal and spatial properties of seeing at Paranal (A), Thermal loading in the VLTI (B), Internal seeing within the VLTI (C), Isoplanatism at Paranal (D), Large scale structure in the atmosphere above Paranal (E), Air flow through the VLTI (F), Performance of STRAP (G), Seismic Activity (H), Model for the refractive index of air (I), Spectral Response of PRIMA Hardware (J), Earth rotation model (K), Position and separation of stars (L), Date and time of the observations (M), Observing parameters (N).
Temporal and spatial properties of seeing at Paranal	A	Large scale structure in the atmosphere above Paranal (E).
Internal seeing within the VLTI	C	Thermal loading in the VLTI (B), Large scale structure in the atmosphere above Paranal (E), Air flow through the VLTI (F).
Isoplanatism at Paranal	D	Large scale structure in the atmosphere above Paranal (E).
Air flow through the VLTI	F	Large scale structure in the atmosphere above Paranal (E).
Performance of STRAP	G	Observing parameters (N).
Earth rotation model	K	Date and time of the observations (M).

Table 8: Table of direct and indirect dependencies.

Term	Section of this document	Other terms directly and indirectly dependent on this (and the appropriate section numbers)
Wavefront amplitude and phase fluctuations above M1	4	Wavefront corrugations before and after the StS (5), Wavefront corrugations before VCM (6), Wavefront corrugations before FSU spatial filter (7), Atmospheric scintillation and thermal background fluctuations (9), Refractive index of air and colour of correlated flux (12), VLTI baseline geometry (15), Systematic differences in baseline length for primary and secondary star (16), Effect of aberrations in image plane optical components (20), Image plane optics in the star separator (21), Effect of aberrations in pupil plane optical components (23), Effect of beam walk on optics before the Star Separator (24), Systematic errors in the FSU phase (25), Total spectral response of PRIMA system (27), Fringe jumps and group tracking errors (28), Limiting magnitudes for PRIMA (29), Total astrometric error (30).
Wavefront corrugations before and after the StS	5	Wavefront corrugations before VCM (6), Wavefront corrugations before FSU spatial filter (7), Atmospheric scintillation and thermal background fluctuations (9), Refractive index of air and colour of correlated flux (12), VLTI baseline geometry (15), Systematic differences in baseline length for primary and secondary star (16), Effect of aberrations in image plane optical components (20), Image plane optics in the star separator (21), Effect of aberrations in pupil plane optical components (23), Effect of beam walk on optics before the Star Separator (24), Systematic errors in the FSU phase (25), Total spectral response of PRIMA system (27), Fringe jumps and group tracking errors (28), Limiting magnitudes for PRIMA (29), Total astrometric error (30).
Wavefront corrugations before VCM	6	Wavefront corrugations before FSU spatial filter (7), Atmospheric scintillation and thermal background fluctuations (9), Refractive index of air and colour of correlated flux (12), VLTI baseline geometry (15), Systematic differences in baseline length for primary and secondary star (16), Effect of aberrations in image plane optical components (20), Systematic errors in the FSU phase (25), Total spectral response of PRIMA system (27), Fringe jumps and group tracking errors (28), Limiting magnitudes for PRIMA (29), Total astrometric error (30).

Wavefront corrugations before FSU spatial filter	7	Atmospheric scintillation and thermal background fluctuations (9), Refractive index of air and colour of correlated flux (12), VLTI baseline geometry (15), Systematic differences in baseline length for primary and secondary star (16), Effect of aberrations in image plane optical components (20), Systematic errors in the FSU phase (25), Total spectral response of PRIMA system (27), Fringe jumps and group tracking errors (28), Limiting magnitudes for PRIMA (29), Total astrometric error (30).
Internal vibration in the VLTI	8	Wavefront corrugations before and after the StS (5), Wavefront corrugations before VCM (6), Wavefront corrugations before FSU spatial filter (7), Atmospheric scintillation and thermal background fluctuations (9), Refractive index of air and colour of correlated flux (12), VLTI baseline geometry (15), Systematic differences in baseline length for primary and secondary star (16), Effect of aberrations in image plane optical components (20), Image plane optics in the star separator (21), Effect of aberrations in pupil plane optical components (23), Effect of beam walk on optics before the Star Separator (24), Systematic errors in the FSU phase (25), Total spectral response of PRIMA system (27), Fringe jumps and group tracking errors (28), Limiting magnitudes for PRIMA (29), Total astrometric error (30).
Atmospheric scintillation and thermal background fluctuations	9	Refractive index of air and colour of correlated flux (12), VLTI baseline geometry (15), Systematic differences in baseline length for primary and secondary star (16), Systematic errors in the FSU phase (25), Total spectral response of PRIMA system (27), Fringe jumps and group tracking errors (28), Limiting magnitudes for PRIMA (29), Total astrometric error (30).
Effect of detector noise and photon shot noise	10	Systematic errors in the FSU phase (25), Fringe jumps and group tracking errors (28), Limiting magnitudes for PRIMA (29), Total astrometric error (30).
Polarisation effects	11	Systematic errors in the FSU phase (25), Total astrometric error (30).
Refractive index of air and colour of correlated flux	12	Fringe jumps and group tracking errors (28), Limiting magnitudes for PRIMA (29), Total astrometric error (30).

Drift in image plane VCMs	13	Atmospheric scintillation and thermal background fluctuations (9), Refractive index of air and colour of correlated flux (12), VLTI baseline geometry (15), Systematic differences in baseline length for primary and secondary star (16), Effect of aberrations in pupil plane optical components (23), Systematic errors in the FSU phase (25), Total spectral response of PRIMA system (27), Fringe jumps and group tracking errors (28), Limiting magnitudes for PRIMA (29), Total astrometric error (30).
VLTI baseline geometry	15	Total astrometric error (30).
Systematic differences in baseline length for primary and secondary star	16	Total astrometric error (30).
Galactic effects	17	Total astrometric error (30).
Solar System effects	18	Total astrometric error (30).
Systematic effects from the atmosphere	19	Total astrometric error (30).
Effect of aberrations in image plane optical components	20	Total astrometric error (30).
Image plane optics in the star separator	21	Total astrometric error (30).
Position error between beam footprints in Star Separator calibration mode	22	Effect of aberrations in image plane optical components (20), Effect of aberrations in pupil plane optical components (23), Total astrometric error (30).
Effect of aberrations in pupil plane optical components	23	Total astrometric error (30).
Effect of beam walk on optics before the Star Separator	24	Total astrometric error (30).
Systematic errors in the FSU phase	25	Total astrometric error (30).
Knowledge of stellar spectra	26	Refractive index of air and colour of correlated flux (12), VLTI baseline geometry (15), Systematic differences in baseline length for primary and secondary star (16), Fringe jumps and group tracking errors (28), Limiting magnitudes for PRIMA (29), Total astrometric error (30).

Total spectral response of PRIMA system	27	Refractive index of air and colour of correlated flux (12), VLTI baseline geometry (15), Systematic differences in baseline length for primary and secondary star (16), Fringe jumps and group tracking errors (28), Limiting magnitudes for PRIMA (29), Total astrometric error (30).
Fringe jumps and group tracking errors	28	Limiting magnitudes for PRIMA (29), Total astrometric error (30).
Temporal and spatial properties of seeing at Paranal	A	Wavefront amplitude and phase fluctuations above M1 (4), Wavefront corrugations before and after the StS (5), Wavefront corrugations before VCM (6), Wavefront corrugations before FSU spatial filter (7), Atmospheric scintillation and thermal background fluctuations (9), Refractive index of air and colour of correlated flux (12), VLTI baseline geometry (15), Systematic differences in baseline length for primary and secondary star (16), Effect of aberrations in image plane optical components (20), Image plane optics in the star separator (21), Effect of aberrations in pupil plane optical components (23), Effect of beam walk on optics before the Star Separator (24), Systematic errors in the FSU phase (25), Total spectral response of PRIMA system (27), Fringe jumps and group tracking errors (28), Limiting magnitudes for PRIMA (29), Total astrometric error (30).
Thermal loading in the VLTI	B	Wavefront corrugations before and after the StS (5), Wavefront corrugations before VCM (6), Wavefront corrugations before FSU spatial filter (7), Atmospheric scintillation and thermal background fluctuations (9), Refractive index of air and colour of correlated flux (12), VLTI baseline geometry (15), Systematic differences in baseline length for primary and secondary star (16), Effect of aberrations in image plane optical components (20), Image plane optics in the star separator (21), Effect of aberrations in pupil plane optical components (23), Effect of beam walk on optics before the Star Separator (24), Systematic errors in the FSU phase (25), Total spectral response of PRIMA system (27), Fringe jumps and group tracking errors (28), Limiting magnitudes for PRIMA (29), Total astrometric error (30), Internal seeing within the VLTI (C).

Internal seeing within the VLTI	C	Wavefront corrugations before and after the StS (5), Wavefront corrugations before VCM (6), Wavefront corrugations before FSU spatial filter (7), Atmospheric scintillation and thermal background fluctuations (9), Refractive index of air and colour of correlated flux (12), VLTI baseline geometry (15), Systematic differences in baseline length for primary and secondary star (16), Effect of aberrations in image plane optical components (20), Image plane optics in the star separator (21), Effect of aberrations in pupil plane optical components (23), Effect of beam walk on optics before the Star Separator (24), Systematic errors in the FSU phase (25), Total spectral response of PRIMA system (27), Fringe jumps and group tracking errors (28), Limiting magnitudes for PRIMA (29), Total astrometric error (30).
Isoplanatism at Paranal	D	Wavefront amplitude and phase fluctuations above M1 (4), Wavefront corrugations before and after the StS (5), Wavefront corrugations before VCM (6), Wavefront corrugations before FSU spatial filter (7), Atmospheric scintillation and thermal background fluctuations (9), Refractive index of air and colour of correlated flux (12), VLTI baseline geometry (15), Systematic differences in baseline length for primary and secondary star (16), Effect of aberrations in image plane optical components (20), Image plane optics in the star separator (21), Effect of aberrations in pupil plane optical components (23), Effect of beam walk on optics before the Star Separator (24), Systematic errors in the FSU phase (25), Total spectral response of PRIMA system (27), Fringe jumps and group tracking errors (28), Limiting magnitudes for PRIMA (29), Total astrometric error (30).

Large scale structure in the atmosphere above Paranal	E	Wavefront amplitude and phase fluctuations above M1 (4), Wavefront corrugations before and after the StS (5), Wavefront corrugations before VCM (6), Wavefront corrugations before FSU spatial filter (7), Atmospheric scintillation and thermal background fluctuations (9), Refractive index of air and colour of correlated flux (12), Drift in image plane VCMs (13), Variation in VLTI fundamental length calibration (14), VLTI baseline geometry (15), Systematic differences in baseline length for primary and secondary star (16), Systematic effects from the atmosphere (19), Effect of aberrations in image plane optical components (20), Image plane optics in the star separator (21), Position error between beam footprints in Star Separator calibration mode (22), Effect of aberrations in pupil plane optical components (23), Effect of beam walk on optics before the Star Separator (24), Systematic errors in the FSU phase (25), Total spectral response of PRIMA system (27), Fringe jumps and group tracking errors (28), Limiting magnitudes for PRIMA (29), Total astrometric error (30), Temporal and spatial properties of seeing at Paranal (A), Internal seeing within the VLTI (C), Isoplanatism at Paranal (D), Air flow through the VLTI (F).
Air flow through the VLTI	F	Wavefront corrugations before and after the StS (5), Wavefront corrugations before VCM (6), Wavefront corrugations before FSU spatial filter (7), Atmospheric scintillation and thermal background fluctuations (9), Refractive index of air and colour of correlated flux (12), VLTI baseline geometry (15), Systematic differences in baseline length for primary and secondary star (16), Effect of aberrations in image plane optical components (20), Image plane optics in the star separator (21), Effect of aberrations in pupil plane optical components (23), Effect of beam walk on optics before the Star Separator (24), Systematic errors in the FSU phase (25), Total spectral response of PRIMA system (27), Fringe jumps and group tracking errors (28), Limiting magnitudes for PRIMA (29), Total astrometric error (30), Internal seeing within the VLTI (C).

Performance of STRAP	G	Wavefront corrugations before and after the StS (5), Wavefront corrugations before VCM (6), Wavefront corrugations before FSU spatial filter (7), Atmospheric scintillation and thermal background fluctuations (9), Refractive index of air and colour of correlated flux (12), VLTI baseline geometry (15), Systematic differences in baseline length for primary and secondary star (16), Effect of aberrations in image plane optical components (20), Image plane optics in the star separator (21), Effect of aberrations in pupil plane optical components (23), Effect of beam walk on optics before the Star Separator (24), Systematic errors in the FSU phase (25), Total spectral response of PRIMA system (27), Fringe jumps and group tracking errors (28), Limiting magnitudes for PRIMA (29), Total astrometric error (30).
Seismic Activity	H	Wavefront corrugations before and after the StS (5), Wavefront corrugations before VCM (6), Wavefront corrugations before FSU spatial filter (7), Internal vibration in the VLTI (8), Atmospheric scintillation and thermal background fluctuations (9), Refractive index of air and colour of correlated flux (12), VLTI baseline geometry (15), Systematic differences in baseline length for primary and secondary star (16), Effect of aberrations in image plane optical components (20), Image plane optics in the star separator (21), Effect of aberrations in pupil plane optical components (23), Effect of beam walk on optics before the Star Separator (24), Systematic errors in the FSU phase (25), Total spectral response of PRIMA system (27), Fringe jumps and group tracking errors (28), Limiting magnitudes for PRIMA (29), Total astrometric error (30).
Model for the refractive index of air	I	Refractive index of air and colour of correlated flux (12), Fringe jumps and group tracking errors (28), Limiting magnitudes for PRIMA (29), Total astrometric error (30).
Spectral Response of PRIMA Hardware	J	Refractive index of air and colour of correlated flux (12), VLTI baseline geometry (15), Systematic differences in baseline length for primary and secondary star (16), Total spectral response of PRIMA system (27), Fringe jumps and group tracking errors (28), Limiting magnitudes for PRIMA (29), Total astrometric error (30).
Earth rotation model	K	VLTI baseline geometry (15), Total astrometric error (30).

Position and separation of stars	L	Wavefront amplitude and phase fluctuations above M1 (4), Wavefront corrugations before and after the StS (5), Wavefront corrugations before VCM (6), Wavefront corrugations before FSU spatial filter (7), Atmospheric scintillation and thermal background fluctuations (9), Refractive index of air and colour of correlated flux (12), VLTI baseline geometry (15), Systematic differences in baseline length for primary and secondary star (16), Galactic effects (17), Solar System effects (18), Effect of aberrations in image plane optical components (20), Image plane optics in the star separator (21), Effect of aberrations in pupil plane optical components (23), Effect of beam walk on optics before the Star Separator (24), Systematic errors in the FSU phase (25), Total spectral response of PRIMA system (27), Fringe jumps and group tracking errors (28), Limiting magnitudes for PRIMA (29), Total astrometric error (30).
Date and time of the observations	M	VLTI baseline geometry (15), Solar System effects (18), Total astrometric error (30), Earth rotation model (K).
Observing parameters	N	Wavefront amplitude and phase fluctuations above M1 (4), Wavefront corrugations before and after the StS (5), Wavefront corrugations before VCM (6), Wavefront corrugations before FSU spatial filter (7), Atmospheric scintillation and thermal background fluctuations (9), Effect of detector noise and photon shot noise (10), Refractive index of air and colour of correlated flux (12), VLTI baseline geometry (15), Systematic differences in baseline length for primary and secondary star (16), Effect of aberrations in image plane optical components (20), Image plane optics in the star separator (21), Effect of aberrations in pupil plane optical components (23), Effect of beam walk on optics before the Star Separator (24), Systematic errors in the FSU phase (25), Total spectral response of PRIMA system (27), Fringe jumps and group tracking errors (28), Limiting magnitudes for PRIMA (29), Total astrometric error (30), Performance of STRAP (G).

Table 9: Table of direct and indirect dependencies.

___oOo___